Relevant changes made to the manuscript

The following is a list of the major changes made to the manuscript in response to the reviewer's constructive feedback:

- Changed the title of the manuscript from "Instabilities within Rotating mode-2 Internal Wave" to "Multi-scale phenomena of rotation modified mode-2 internal waves".
- Improved the motivation for the Schmidt number dependence section.
- Clarification of the use of the term DNS.
- Additional comments regarding the characterization of the leading wave.
- Expanded the discussion on the applicability of the resolution used in our simulations.
- Compared the length and times scales of the shear instabilities for different cases.

Reviewer 1 Response

David Deepwell, Marek Stastna, Aaron Coutino

January 30, 2018

We thank the Reviewers for their comments. We have responded to all comments, and where applicable have added in their feedback into the article. Reviewer comments are in bold font, responses are in normal font.

Page 3, Line 11: I do not think the authors conducted DNS as they claim in line 11. For such kind of simulations the grid step should be at the level of the Kolmogorov's scale, but there are no details on both in the text. And what about numerical viscosity? With quite a coarse grid it can be several order higher than the molecular viscosity, $2 \times 10^{-6} \mathbf{m^2/sec}$, as claimed in the paper.

The text has been modified to include the following paragraph addressing this issue: "We have run a series of direct numerical simulations (DNS) in a setup similar to that of Maxworthy (1983), who employed a gravity intrusion from a lock release in a rotating, rectangular tank to generate mode-2 waves. Since the flow develops from a state of rest the precise definition of the term "Direct Numerical Simulation" from the turbulence literature, namely that grid spacing must be smaller than the Kolmogorov microscale, cannot be directly translated to the present situation. We define DNS in the sense commonly adopted in the stratified flow modeling literature, with Arthur and Fringer (2016) providing a concrete example. These authors state that DNS is a three-dimensional simulation which has a grid spacing which is "within approximately one order of magnitude of the Kolmogorov length scale". The Kolmogorov scale for transitional flows is defined in an ad hoc manner, usually via the explicit calculation of the viscous dissipation rate. The grid scale of our simulations is comparable to this usage since it is within an order of magnitude of the Kolmogorov scale defined from the maximum local dissipation rate. Moreover, our numerical method is spectral, and hence higher order than that used in Arthur and Fringer (2016). The spectral filter used control aliasing applies only to the largest 30% of wavenumbers and leaves the majority untouched, and no subgrid scale model as in Large Eddy Simulation (LES) is used. In the absence of a better term, DNS will be used throughout."

Page 4, line 8: The authors take the first-mode phase speed as the velocity scale, although the whole model set-up is for the 2nd mode experiments. Does this make sense?

The presented velocity scale is the correct mode-2 phase speed rather than the mode-1 phase speed. We have clarified this point in the manuscript to remove further confusion.

I'm not sure I understand the meaning of two concepts, c_w and a_w. They are

introduced in line 2 on page 4 in a very general way, without clear explanation how do they relate to the model set-up. However, they appear in table 2 as input parameters. What is the link of these values with the tank experiment parameters (size scales, stratification parameters, rotation, etc)?

c_w and a_w are characterizations (not initial parameters) of the resultant mode-2 ISW which describe the measured amplitude and wave speed along the focusing wall. a_w is related to the depth of the initial perturbation, H_m, while c_w is amplitude dependent. a_w and c_w have maxima along the focusing wall and have their values decrease along a normal to this surface. The choice of a_w and c_w was made following Maxworthy (1982). We have included a short discussion and included additional references on how these parameters are associated with tank experiment parameters.

And why the wave speed, as it is introduced on page 4, is larger than the fastest mode 1 wave speed c_0? It seems to me the authors did not pay much attention how their paper will be accepted by the readers.

The wave speed is faster than the linear, mode-2, long wave speed because these waves are highly non-linear and have a strong amplitude dependence. This is a result for finite amplitude mode-2 waves (see Terez and Knio (1998), Brandt and Shipley (2014), or Salloum et al. (2012)). For clarity, we have added a comment about the amplitude dependence of the wave speed which leads to this larger value.

Relatively minor, but important: The presented on page 5 system is not the NS-system as stated.

We have fixed this.

Please, be careful defining the total water density and its perturbations. Secondly, the temperature, salinity and the EoS are the constituents of the NS-type system, but not the density perturbation (find also a mistake in the first eqn.)

We have explained the set of governing equations used and their relation to the set of equations believed to apply to the oceanic situation: "The equations used differ from the oceanic situation in that we take the density as a variable to be evolved, where as in the ocean it is the salinity and temperature that evolve, with density recovered from an equation of state. The nonlinearity of the equation of state leads to a variety of complex phenomena (e.g. salt fingering, cabbeling, the fact that pure water has a density maximum at 4 degrees Centigrade, etc). In the laboratory, density changes are typically imposed by variations in salinity with the temperature held fixed. Our formulation mirrors this situation, though the experimentally observed diffusivity of salt proves too low for inclusion in the numerical simulations."

The set of equations we use is standard throughout the literature, but the distinction with the oceanic situation is worth discussion.

I'm not sure why do the author change the Sc number? They call it the Schmidt number (why not the Prandtl number?, but never mind) and vary it from 1 to 10. This does not make any sense if the authors conduct their experiments for the laminar-size grid. The viscosity and diffusivity coefficients are constant at the Kolmogorov scale level (laminar!!), so why the authors considered their ten times variation (Table 2)? What is the idea behind that?

We have rewritten the introduction so as to have the reason for varying the Schmidt number be clear at the outset. An extract from this paragraph reads: "In terms of the numerical modeling literature, we are interested in exploring how the Schmidt number (or Prandtl number in thermally stratified systems) affects the localized shear instabilities generated near the Kelvin wave crest. This

is important since Schmidt numbers representative of salt stratification (Sc $\approx$ 700) are presently intractable for numerical simulations on all but the smallest scales, but realistic results may be obtained by choosing a Schmidt number larger than that for a heat stratified system (Sc $\approx$ 7) but much smaller than that of salt. It also implies that while field scale simulations like those of Sanchez-Garrido and Vlasenko (2009) may have a similar Rossby number to an experimental study, they cannot have the same viscosity and diffusivity, implying that experimentalists need to carefully assess what aspects of such simulations they may successfully observe in the laboratory."

Finally, what is the spatial grid resolution after all? Looking at Table 3 I can see it is at the level of 10^{-3} m (i.e. 1mm), which is small, but does not tell me whether this is small enough for replication of the laboratory-scale experiments and the background mixing. Maybe yes, but the text in its present state is not convincing enough for me.

We have added "For the resolution listed in table 3, the strongly stratified region of the background stratification contains approximately, $2h/\Delta z \approx 33$ points, while the entire stratification has approximately 140 points. Small scale features in the transitional flow typically are a couple centimetres in diameter and contain about 20 points. The applicability of the stated resolution was also found by comparing the grid scale to the Kolmogorov scale which we define using the maximum local energy dissipation rate. In all cases the maximum grid resolution is within an order of magnitude of the Kolmogorov scale. Thus, our simulations are well resolved."

No details are provided how the initial ISW was created. Figure 1 does show the initial installation, and I can believe that in the vertically symmetrical case the leading ISW is a second mode wave, but it really takes time to form in the front of the wave field. Is 6.4m tank long enough to form it? When the rotation has been switched on? Right in the beginning of the experiment? What is the idea of all these experiments? I would accept the method of initial wave formation and initiation of the rotation after that to learn the effect of rotation, but all the details must be explained. I'm really confused without the correct setting of the experiment conditions. Lines 15-25 on page 6 do not bring any clearance on this point.

It was assumed that a reader either has a prior knowledge of tank scale mode-2 experiments or is prepared to follow some of the references provided, but obviously this needed to be cleared up. Based on the reviewer comment, we have ensured that some discussion of the lock-release generation method is provided and that sufficient references have now been given which explain in detail the process by which the ISW is formed. For the initial conditions of the manuscript, the resultant mode-2 ISW is essentially formed within a meter of the collapse region. This is sufficiently quick and leaves the majority of the tank to be used as the domain for the rotation affected ISW. The rotation is present from the moment the simulation begins (as would be the case in a laboratory realization of our numerical set up). Lines 15-25 on page 6 describe a way to measure the location of the wave front in the x-y plane by tracking the kinetic energy. This is used to show the span-wise variation in the ISW rather than the vertical variation which is normally done.

Reviewer 2 Response

David Deepwell, Marek Stastna, Aaron Coutino

January 30, 2018

We thank the Reviewers for their comments. We have attempted to respond to all comments. In the case of Reviewer 2, some very insightful comments require computational resources/computation time beyond the one-month revision period and we have taken these as suggestion for future work. Reviewer comments are in bold font, responses are in normal font.

1 Major comments

There is no comparison between the numerical results and field observations, or attempts to suggests how and where the processes discussed in this manuscripts could be observed in nature. I think is relevant to motivate the readers with some realistic applications of the paper's outcomes. For instance, the authors might compare their numerical experiments in the absence of rotation with the laboratory experiments performed by Carr et al. (2015), since they have collaborated on recent work (Deepwell et al. 2017).

The reviewer is correct that we were not very clear on this point. We have added a paragraph to the introduction that outlines where we see our study in terms of field, experimental and numerical approaches:

"Results on non-rotating mode-2 ISWs, especially with regards to their mass transport capabilities (Deepwell and Stastna (2016), Salloum et al (2012), Brandt and Shipley (2014), Terez and Knio (1998)), are readily available and there is considerable contact between the experimental and numerical modeling literature. This is exemplified by recent progress on quantifying the effects of displacing the pycnocline center from the mid-depth (Carr et al. (2015), Olsthoorn et al. (2013)). In contrast, mode-2 ISWs in a rotating reference frame have been document experimentally by Maxworthy (1983), but no high resolution numerical simulations that provide concrete examples of phenomena future experimental efforts could aim to document exist. We provide such simulations below, with a focus on the overturning induced by the rotation modified ISW (or Kelvin wave, depending on one's choice of terminology) at the focusing boundary.

Our primary qualitative results that could be confirmed in the laboratory concern the fundamentally three dimensional nature of the shear instability at the edges of the mode-2 wave's core, and the the details of the spatial structure of the span-wise kinetic energy flux. The former could be visualized by a PIV system with a light sheet oriented in the span-wise direction, while the

latter could be characterized by the more usual along-tank PIV set up. Moreover, the quantitative results of the Kelvin wave-Poincaré wave resonance and the formation of secondary Kelvin waves in our simulation should provide an easier comparison than field oriented simulations such as those of Sanchez-Garrido and Vlasenko (2009). In terms of the numerical modeling literature, we are interested in exploring how the Schmidt number (or Prandtl number in thermally stratified systems) affects the localized shear instabilities generated near the Kelvin wave crest. This is important since Schmidt numbers representative of salt stratification ($Sc \approx 700$) are presently intractable for numerical simulations on all but the smallest scales, but realistic results may be obtained by choosing a Schmidt number larger than that for a heat stratified system ($Sc \approx 7$) but much smaller than that of salt. It also implies that while field scale simulations like those of Sanchez-Garrido and Vlasenko (2009) may have a similar Rossby number to an experimental study, they cannot have the same viscosity and diffusivity, implying that experimentalists need to carefully assess what aspects of such simulations they may successfully observe in the laboratory."

The authors do not discuss the implications of the free-slip boundary conditions adopted in their numerical experiments; this is the case of Maxworthy (1983). For instance, how does the growth of shear instabilities near no-slip walls would change the results?

Free slip boundaries are the commonly adopted first choice in numerical studies. No slip boundaries, and the clustered Chebyshev grids necessary to resolve them, would greatly increase the expense of the simulations. We believe that a no-slip boundary condition will have minimal impact on the Kelvin wave and on the shear instabilities near the wall, because the length scales of these instabilities are significantly larger than the boundary layer thickness. We have added a comment to the text, but carrying out no slip simulations is certainly an important future direction.

The authors explore only one background stratification aspect ratio h1=h2, h, with different wave amplitudes. I wonder why they did not explore other background stratification. I would expect that in nature an upper layer thinner than a deep layer, or vice-versa. It might be interesting to explore how the asymmetry in layer thicknesses would change the growth and structure of K-H like instabilities.

It is correct that nature typically has stratifications which consist of a thick deep layer and a thinner upper layer, but this break in the symmetry of layer depth leads to far more complicated behaviour (see Olsthoorn et al. (2013) and Carr et al. (2015)) coupling mode-2 and mode-1 wave generation. We decided, as many authors have in the literature on mode-2 ISWs, to begin with the simple first case of equal layer depths. We have included a comment on this in the article, and mention that unequal layer depths is a possible avenue for further investigation.

The title of the article suggests that the focus of the manuscript is the transition to turbulence driven by second vertical mode internal waves in a rotating environment, but the paper is more general than this title. The paper examines the macro- and micro-scale processes driven by the degeneration of second vertical mode solitary waves in a rotating and bounded stratified flow. I would suggest the authors think of a different title.

The title has been changed to "Multi-scale phenomena of rotation modified mode-2 internal waves".

2 Specific Comments

1. In the introduction, one would also cite the work by Moum et al. (2003) or more recent observations by Zhang and Alford (2015), and for motivations, for instance, Cuypers et al. (2010).

We have added references to these articles in the introduction.

2. On page 2, between 20 and 25, I would mention the results obtained by Melville et al. (1989).

We have done so. This was a necessary inclusion in this article.

3. How did you estimate that a single turbulent patch has a vertical extent of about 40 cm, where are the 25 points coming from? Vertical grid points? Are the authors making a reference to Ulloa et al. (2015)'s paper?

Yes, we are referencing Ulloa et al. (2015) in measuring their turbulent patch. We estimated that the vertical extent of the patch was 0.04 m. With a vertical grid spacing of 1.55 mm this would give a total of 25 grid points in the region. We have decided to remove the discussion on the resolution of the turbulent patch since it doesn't add anything to the current article and makes sense to revisit in future work.

4. Subsections 1.1 and 1.2: Why equations are not enumerated? Please, enumerate them.

We have done so.

5. Page 3, paragraph 20: It seems obvious, but the authors could write that the domain is Lx x Ly x Lz = 6.4 m x 0.4 m x 0.3 m, or something like that.

We have done so.

6. Table 1: Missing units of z0 and h; both variable should be defined and schematised in Figure 1.

The definition and units of the variables have been included. The schematic has been unchanged since the addition would cause too much clutter to the plot.

7. Page 4, paragraph 10: ' ... we attempt to carry out a Direct Numerical Simulation (DNS) ... '. Concerning this sentence, what is the Kolmogorov scale of the numerical experiments? What is the Ozmidov scale? If authors are solving the Kolmogorov scale, please take the word 'attempt' out of the sentence, otherwise explain further.

The text has been modified to include the following paragraph addressing this issue:

"We have run a series of direct numerical simulations (DNS) in a setup similar to that of Maxworthy (1983), who employed a gravity intrusion from a lock release in a rotating, rectangular tank to generate mode-2 waves. Since the flow develops from a state of rest the precise definition of the term "Direct Numerical Simulation" from the turbulence literature, namely that grid spacing must be smaller than the Kolmogorov microscale, cannot be directly translated to the present situation. We define DNS in the sense commonly adopted in the stratified flow modeling literature, with Arthur and Fringer (2016) providing a concrete example. These authors state that DNS is a three-dimensional simulation which has a grid spacing which is "within approximately one order of magnitude of the Kolmogorov length scale". The Kolmogorov scale for transitional flows is defined in an ad hoc manner, usually via the explicit calculation of the viscous dissipation rate. The grid scale of our simulations is comparable to this usage since it is within an order of magnitude of the Kolmogorov scale defined from the maximum local dissipation rate. Moreover, our numerical method is spectral in all directions, and hence formally higher order than that used in Arthur

and Fringer (2016). The spectral filter used to control aliasing applies only to the largest 30% of wave numbers and leaves the majority untouched, and no subgrid scale model as in Large Eddy Simulation (LES) is used. Based on these considerations, and in the absence of a better term, DNS will be used throughout."

8. Page 4, paragraph 10: Did Sanchez-Garrido and Vlasenko (2009) define in the same way the Rossby number? It seems that their Rossby number is almost twice smaller than the smaller Ro considered in this work.

Sanchez-Garrido and Vlasenko (2009) do not define a Rossby number or Rossby radius of deformation. An estimate based on the latitude, wave speed, and channel width does give a smaller Rossby number than the one we present, however, we are not attempting to make a direct comparison to a specific geographic region. Comparison to experiments such as those carried out by Grimshaw et al. (2013) gives similar Rossby numbers.

9. Table 2 is referenced in page 4; so far there is no clear explanation about how cw and aw were estimated. The authors explained these parameters were parametrised on the wall, y = 0 m, and the amplitude was defined before the formation of instabilities. Was the emergence of interfacial instabilities defined by visual inspection of the isopycnals? How was then estimated the phase speed, cw? This matter requires a bit of further explanation.

The initial discussion of these parameters was fairly terse, and we have now expanded their discussion and included a reference to a schematic in a previous paper. The main points (as they are now in the paper) are: a_w is measured as the average maximum displacement from the upstream value of the isopycnal $\rho(z_0 \pm h)$. c_w is the speed of the location of this maximum displacement. Yes, the instabilities were visually inspected from the density field.

10. Subsection 1.2: I would suggest rewriting the description of the governing equations. I would suggest something like 'our numerical model solve the Boussinesq equations of motion on an f-plane ...'. 'stratified Navier-Stokes equations' sounds a bit unusual.

We have done so.

11. Page 5, paragraph 15: Is SPINS the acronym given to the numerical solver or is a general pseudo-spectral method?

SPINS is the acronym for the numerical solver. We have fixed the typo in calling it a method as it is actually a particular solver.

12. Page 6, paragraph 5: What type of computational resources were used to perform the numerical experiments (machine, number of cores, computational time)?

A typical run completed in approximately 3 days on 64 processors on Compute Canada resources (SHARCNET). The higher resolution cases required significantly more resources, approximately two weeks using a combination of 64 and 128 processors (either number was used on a restart). Data analysis requiring a day or two added additional computation time. The supercomputer cluster is mentioned in the Acknowledgments.

13. Page 6, paragraph 5: How many vertical grid points does the numerical experiment use to solve the peaks of the square of the buoyancy frequency, N2, on the initial solitary wave? I would include this information to show that the density transitions are well solved. For instance, the vertical length-scale of the pycnocline thickness in the wavefront, h, is solved by around 17 and 36 grid points each vertical grid resolution, respectively.

Yes, we should have discussed the resolution of the stratification. We have added the following sentences to clarify this: "For the resolution listed in table 3, the strongly stratified region of the background stratification contains approximately, $2h/\Delta z \approx 33$ points. The entire stratification has approximately 140 points, and is thus well resolved."

14. Section 2. The authors start refereeing the work of Maxworthy (1983). Similarly to ?, I would compute the relationship between wave amplitude, Aw, phase celerity, cw, and the dependence with the controlling parameter, the Rossby number (and later with the Schmidt number). These results can be discussed along with Figure 3.

Based on the information in table 2 we have added the following discussion: "The wave speed, measured as the speed of the location of the maximum displacement, is independent of the rotation rate and has a value larger than the linear long wave speed due to the large amplitude nature of these waves. The amplitude is only weakly dependent on the rotation rate or Rossby number."

15. Equation 1. The definition of ξ does not allow a quantitative comparison between the numerical experiments. I would recommend using a scaling that allows comparison.

We are concerned with comparing the geometric structure of the waves between different simulations, thus the maximum-scaled KE is the best choice. We have included the maximum unscaled values in the caption for comparison.

16. Page 6, paragraph 25. Where does the shear reach its maximum? at $\widetilde{y} = 0$?

Yes, the shear reaches its maximum at y=0. This has been made clearer in the article.

17. Figure 3: I would include the Rossby number for each experiment to show the background rotation environment along with the resulting wave dynamics.

The Rossby numbers have been added to the figure caption.

18. Section 2 (Page 7, paragraph 5) How did the authors compute the energy partition between Kelvin and Poincar waves? The authors may compute spatial spectra as a function of time to quantify the energy contained in the spanwise and streamwise axes.

We agree that the sentence, as written, was confusing. We have replaced it with: "Overall, the spatial distribution of kinetic energy is dominated by the Kelvin wave front and two secondary features near the focusing wall." This re-write is based on the observations made in figure 3. We note that because of the curvature of the Kelvin wave front, a spanwise spectrum will not provide an accurate representation of the energy.

19. Page 8, paragraph 10. How is this Kelvin-Poincar wave resonance compared with the one studied by Melville et al. (1989), and the observed by Renouard et al. (1993). It seems that the train of solitary waves obtained by Ulloa et al. (2015) also converges to azimuthal secondary Kelvin waves.

In Renouard et al. (1993) the Poincare waves were resonantly generated as the ISW turned at a right-angled corner. We have added the following sentences:

"Renouard et al. (1986), however, matches our results of Poincare waves being resonantly generated along the side wall. Melville et al. (1989) also clearly shows that the curvature of the wave front is due to the combination of a Poincare and Kelvin wave. Our results are in agreement with both of these results, but now applying to mode-2 ISWs."

20. Page 9, paragraph 10: Is there any experimental evidence that a secondary Kelvin wave becomes more energetic and overtakes the leading Kelvin wave? What

is the relevance of this phenomenon? This might be possible to show, for instance, by using a circular basin such as those used by Wake et al. (2005) and Ulloa et al. (2014). However, this would be a different problem. I think the authors should emphasize the relevance and implications of having secondary Kelvin waves in the system.

We are unaware of any experimental evidence showing secondary waves surpassing the leading Kelvin wave. For rectangular geometry, this is likely to remain the case as it takes considerable time for the transfer of energy to occur. Circular basins are a different problem with additional effects due to the curvature of the side walls. We have added this point into the article.

21. Page 12, paragraph 5: Is there any relationship between the internal Rossby radius of deformation and the length-scale where shear instabilities were found in the spanwise direction? The authors state that this region is confined to a quarter of the transversal length-scale, Lz. However, did they observe any change in terms of the Rossby radii?

Yes, the Rossby number does play a role in determining the length-scale of the instabilities. We've added a discussion on this result.

22. Page 12, paragraph 10: Why did the oscillatory K-H like billows disappear once the vertical resolution was increased? Any further thought? What was the most critical wavenumber in both cases, when nz = 256, and nz = 512. The authors could perform a stability analysis to understand the nature of the instabilities and the growth rate.

For clarity, we note that the billows do not "disappear", but that small details of their evolution change. We have begun a more systematic study of even higher resolution simulations of this, and a number of other, studies in order to unravel some of the subtle ways in which hydrodynamic instability and numerical viscosity interact. Since such simulations take a long time we have cut down some of the discussion in the present manuscript. The suggestions given by the reviewer here will be taken into account in the future study. The background state is quite complex (i.e. it is not a parallel shear flow, see figure demonstrating non-negligible vertical velocity (in m/s) at focusing wall in case 10_1 below), and hence a detailed stability analysis, while a good idea, is really a separate study. (figure 1 here).

23. Page 12, paragraph 10: Regarding the von-Karman like vortices. I would think that this kind of instabilities is possible to have a physical sense. There is a localised solitary wave propagating through a mid-layer in an initially quiescent stratified fluid. If we move on the leading solitary wave on the near-wall zone, the solitary wave feels there is a streamwise flow in the opposite direction. This scenario leads to a shear flow that could be similar than the one observed in the generation of von-Karman street vortices. Could you please give a look at the vertical velocity profile along the core of the leading wave?

We have added the following: "These K-H billows can also be considered analogous to a von Karman vortex street. In a reference frame moving with the wave, the background flow is directed around the wave, much like it is around a cylinder in von Karman's classical experiment. The analogy is somewhat limited since the Kelvin wave core is not a solid, and due to the rotation the core bends backward away from the wall (and hence isn't a cylinder). Moreover, the instability is a shear instability, as opposed to a boundary layer separation." We have looked at the velocity, but have not included this figure in the manuscript since the density figures makes the vortices quite apparent. (Figure 2 here)

24. Page 13, paragraph 5: Is there any clue of baroclinic-like instabilities? Have the authors observed the vorticity field in the x -y plane?

We have looked at the vorticity field and find no evidence of baroclinic-like instabilities. We have also done a back-of-the-envelope calculation for the fastest growing baroclinic mode and find that the scale of the waves in the manuscript is smaller than typical baroclinic disturbances by more than an order of magnitude.

25. Page 14, paragraph 10: Did the authors compute the local gradient Richardson numbers on the leading solitary wave zone?

Yes, we did. We have added the following sentence: "Though the Richardson number is not applicable in the upper and lower layers where there is no vertical density variation, within the wave core the Richardson number drops below 1/4 around the edge of the mode-2 bulge while the K-H billows form."

26. Page 16, paragraph 10: Do the authors think that the channel width plays any role in the train of solitary-type waves structure and the shear instabilities growth? If so, please comment.

For the instability of the leading Kelvin wave, the highest rotation rate case shows that the instability occurs within 10 cm of the focusing wall (approximately a quarter of the channel width used). Thus in fact a narrower tank would give similar results. Since the trailing Poincare and Kelvin waves are a result of the leading wave we expect them to have no impact on the shear instabilities of the leading wave. The width of the channel will, however, adjust the reflection of the Poincare waves and thus the resonance of the secondary Kelvin wave. This last point has been included.

27. Page 17, paragraph 10: What grid resolution would be required to solve the Batchelor scale in a numerical experiment with Sc=700? How far are we to solve this problem?

Our Kolmogorov scale (as defined from the maximum local dissipation rate) is approximately 2.5e-4 m. The Batchelor scale is therefore approximately 1e-5 m for Sc=700. For our domain size (6.4x0.4x0.3) this would require about 7.5e14 total points. At our highest resolution we use about 5e8 total points. Hence, we are still a very long way from resolving the Sc=700 case.

28. Page 18, paragraph 10: 'Since the stratification has broadened in this case, the Richardson number has increased leaving the unstable region for shear instabilities to form.' Please, explain better this sentence.

The meaning in this was certainly unclear. We have changed it to read: "The higher diffusivity in the Sc = 1 case acts to hinder the production of shear instabilities by quickly diffusing them as they form."

29. Results: Schmidt number dependence. What is the message from this section? In a thermally stratified fluid (Pr=7) we could expect dynamics such as those shown in Figure 14(a,b).

We were not as clear as we could have been in the purpose of the Schmidt number dependence section. The following sentences have been included in the introduction to motivate this better.

"In terms of the numerical modeling literature, we are interested in exploring how the Schmidt number (or Prandtl number in thermally stratified systems) affects the localized shear instabilities generated near the Kelvin wave crest. This is important since Schmidt numbers representative of salt stratification (Sc $\approx$ 700) are presently intractable for numerical simulations on all but the smallest scales, but realistic results may be obtained by choosing a Schmidt number larger than

that for a heat stratified system (Sc $\approx$ 7) but much smaller than that of salt. It also implies that while field scale simulations like those of Sanchez-Garrido and Vlasenko (2009) may have a similar Rossby number to an experimental study, they cannot have the same viscosity and diffusivity, implying that experimentalists need to carefully assess what aspects of such simulations they may successfully observe in the laboratory."

30. There is a problem with the references, the doi link is duplicated.

Unfortunately this is a problem with the Copernicus bibliography style. We have done what we can to fix it.

31. Abstract: I do not understand what does the last sentence mean: 'Comparisons of equivalent cases with different Schmidt numbers indicate that while low Schmidt number results in the correct general characteristics of the modified ISWs, it does not correctly predict the trailing Poincar wave field or the intensity and duration of the K-H instabilities'. What is not possible to predict at low Schmidt number (guessing the authors refer to Sc = 1)? How are the authors predicting the trailing Poincar wave field and the intensity and duration of K-H instabilities?

We have re-written the abstract to clarify this point. We had unwisely used the word 'predict' when 'model' would have been a better choice. By this we mean that a low Schmidt number does not accurately model what we have observed in the higher Schmidt number cases.

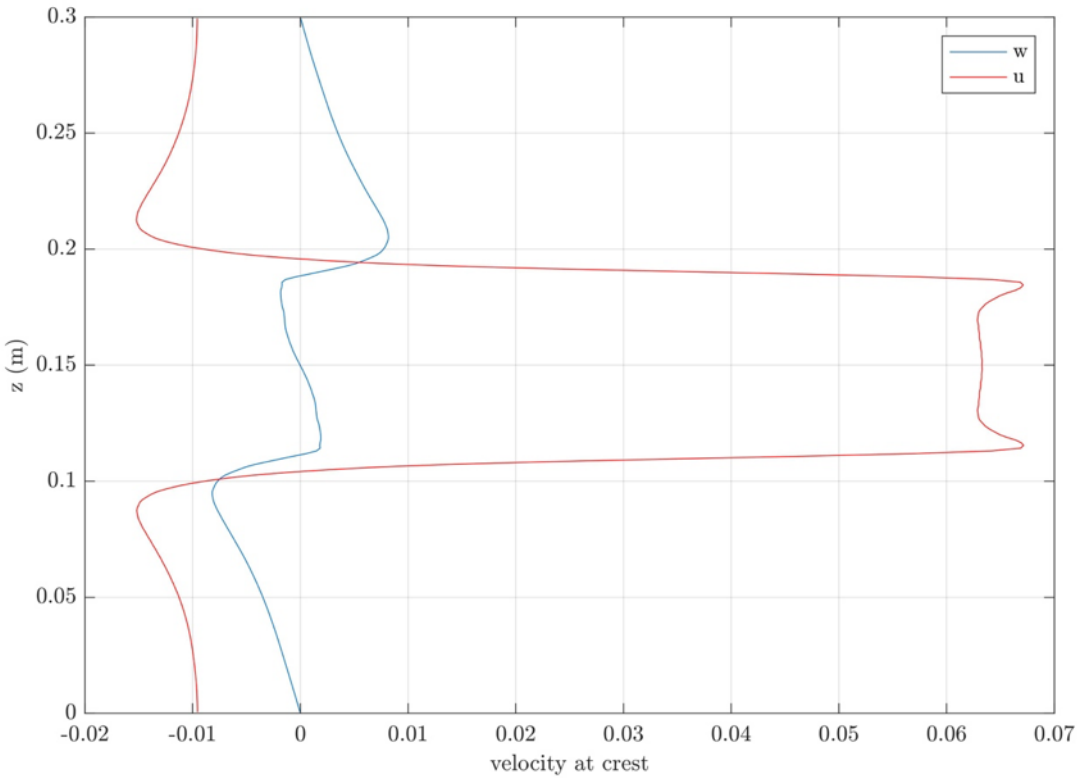
w
u
z (m)
velocity at crest
0.3
0.25
0.2
0.15
0.1
0.05
0
-0.02
-0.01
0
0.01
0.02
0.03
0.04
0.05
0.06
0.07

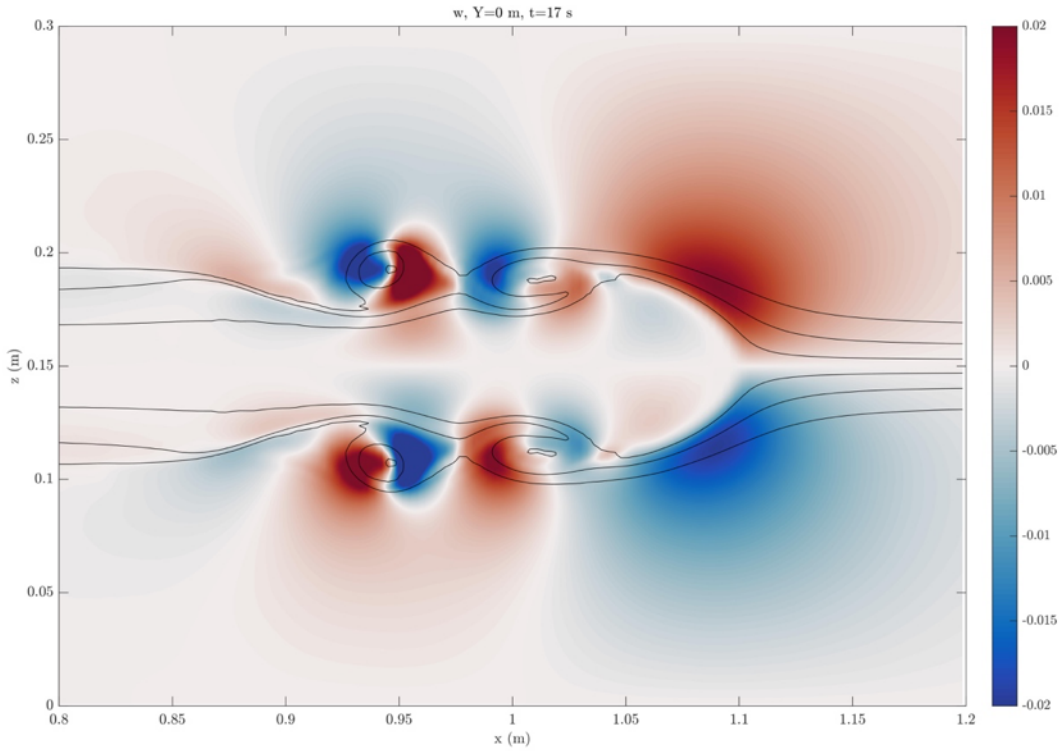
w, Y=0 m, t=17 s
z (m)
x (m)
0.3
0.25
0.2
0.15
0.1
0.05
0
0.8
0.85
0.9
0.95
1
1.05
1.1
1.15
1.2
0.02
0.015
0.01
0.005
0
-0.005
-0.01
-0.015
-0.02

~~Instabilities within Rotating~~ Multi-scale phenomena of rotation modified mode-2 ~~Internal Waves~~internal waves

David Deepwell[1], Marek Stastna[1], and Aaron Coutino[1]

[1]Department of Applied Mathematics, University of Waterloo, Waterloo, Canada

Correspondence to: David Deepwell (ddeepwel@uwaterloo.ca)

Abstract. We present high resolution, three dimensional simulations of rotation modified mode-2 internal solitary waves at various rotation rates and Schmidt numbers. Rotation is seen to change the internal solitary-like waves observed in the absence of rotation into a leading Kelvin wave followed by Poincaré waves. Mass and energy is found to be advected towards the right-most side wall (for Northern hemisphere rotation)~~which led to Kelvin-Helmholtz instabilities within~~ , leading to increased amplitude of the leading Kelvin wave ~~that form above and below the~~ and the formation of Kelvin-Helmholtz instabilities on the upper and lower edges of the deformed pycnocline. These fundamentally three dimensional instabilities are localized within a region near the side wall, and intensify in vigour with increasing rotation rate. Secondary Kelvin waves form further behind the wave from either resonance with radiating Poincaré waves or the remnants of the K-H instability. The first of these mechanisms is in accord with published work on mode-1 Kelvin waves, the second is, to the best of our knowledge, novel to the present study. Both types of secondary Kelvin waves form on the same side of the channel as the leading Kelvin wave. Comparisons of equivalent cases with different Schmidt numbers indicate that while adopting a numerically advantageous low Schmidt number results in the correct general characteristics of the ~~modified ISWs, it does not correctly predict the~~ Kelvin waves, excessive diffusion of the pycnocline and various density features precludes accurate representation of both the trailing Poincaré wave field ~~or~~ and the intensity and duration of the ~~K-H~~ Kelvin-Helmholtz instabilities.

1 Introduction

Over recent decades nonlinear internal solitary waves (ISWs) have been the subject of continuing research due, in part, to their common presence in coastal waters (Shroyer et al. (2010)~~and Lamb (2004)~~, Lamb (2004), and Zhang et al. (2015)) and estuaries (Bourgault and Kelley (2003)), and an expanding set of applications, such as plankton and krill transport (Scotti and Pineda (2004),Cuypers et al. (2010)) or cross-shelf transport (Hosegood and van Haren (2004)). Of particular interest are the effects that rotation has on these waves, since they have been observed to have lifetimes such that this effect is non-negligible (Farmer et al. (2009)). At observation sites such as Knight inset (Klymak and Gregg (2001)) and within the St. Lawrence river (Mertz and Gratton (2013)), side walls may also impact the propagation of these waves. Indeed, classical linear wave theory for rotation modified waves demonstrates that the presence of side walls allows a different type of wave to be created, namely a Kelvin wave.

The dominant laboratory insights on Kelvin waves in a channel geometry come from the experimental work of Maxworthy (1983), and Renouard et al. (1987). These authors performed lab-scale experiments in which mode-2 (Maxworthy (1983)) and mode-1 (Renouard et al. (1987)) Kelvin waves were generated in a rectangular domain. ~~They~~ Both authors found that though the wave amplitude increased at the channel wall with increasing rotation rate, the phase speed and shape were comparable to waves of similar amplitude in the presence of no rotation. The authors also described how the wave amplitude decayed exponentially away from the wall, how the wave front was curved backwards, and how the waves decayed as they propagated away from the generation site due to the generation of inertial waves. Melville et al. (1989) followed this by showing that Poincaré waves of comparable phase speed to a Kelvin wave will naturally resonant with the Kelvin wave, thus causing the curvature of the wave front and the amplitude decay away from the side wall.

In Sánchez-Garrido and Vlasenko (2009) the authors discussed numerical simulations constructed to approximately model the evolution of mode-1 waves in the Strait of Gibraltar. When the latitude was increased to 60 degrees, the authors found clear evidence of a secondary tail of Poincaré waves which trailed the leading Kelvin wave and extracted energy from this wave. The authors also found clear evidence of Mach stems. As this study provides a direct comparison work to our own, its results will be discussed at various points in the following. Observation of mode-1 ISW breaking in a non-rotating environment has been presented by Moum et al. (2003). The authors show that localized increases in stratification (a compression of isopycnals) at the wave crest is followed by interfacial overturning and a breakdown to turbulence.

In the simpler case of a rotating fluid adjusting without the presence of side walls, it has been observed that if dispersive effects are accounted for, a leading solitary wave is created which then breaks down into a nonlinear wave packet as it propagates (Coutino and Stastna (2017)). Additionally, a geostrophic state is created at the site of the initial condition which oscillates at a near inertial frequency and radiates waves. Previous work based on hydrostatic equations (Kuo and Polvani (1997)) had suggested that the nonlinear waves created would steepen and eventually break, however, when dispersive effects are accounted for, breaking does not occur and a nonlinear wave packet is generated instead. This effect has been observed in lab scale experiments using the Coriolis Rotating Platform in Grenoble (Grimshaw et al. (2013)). To ~~account for~~ numerically model these effects the authors used model equations based on the rotation modified Korteweg-de Vries (KdV) or Ostrovsky equation, which gave qualitatively similar results to the observations. However, these equations do not account for the full nonlinearity ~~which accounts for the differences to~~ and dispersion. This accounts for some of the differences with the results in Coutino and Stastna (2017) where the full stratified Euler equations were used.

The work by Fedorov and Melville (1995) showed that if dispersive effects are neglected (when nonlinearity is large), the Kelvin waves will break. Specifically, the authors found that rotation delays the onset of breaking by 60%. When the breaking occurs, it simultaneously forms across the zone of uniform phase that is normal to the boundary. The increase in nonlinearity is seen to create a dipole structure in the cross-shelf velocities. On a similar note, (Kuo and Polvani (1997)) note that ~~time to~~ the time of breaking depends on both the rotation rate and the steepness of the initial conditions (see their ~~Figure~~ figure 18 for details). However, it is unclear how a more realistic model with short wave dispersion would modify these results.

There have been a number of studies on Kelvin waves from a model equation approach. Grimshaw (1985) derived a rotation-modified Korteweg-de Vries (rKdV) equation whose transverse structure is that of a linear Kelvin wave. The author also

showed that when rotation is weak, (the internal Rossby radius is much larger than the wavelength of the wave) the evolution is described by the rotation-modified Kadomstev-Petviashvili (rKP) equation. This was followed up by Katsis and Akylas (1987) who performed a numerical simulation of these equations and found that the wave amplitude varied exponentially across the channel and the wave front was curved backwards in agreement with the results seen in Maxworthy (1983) and Renouard et al. (1987).

Rotation modified mode-1 ISWs within a cylindrical geometry have ~~also~~ been investigated by Ulloa et al. (2014) and Ulloa et al. (2015) using an immersed boundary numerical method. The authors found that the rotation rate affected the nonlinear steepening which further caused a degeneration of the fundamental Kelvin wave into a solitary-type wave packet. When the Kelvin wave amplitude was large enough, localized turbulent patches were produced by Kelvin wave breaking. ~~However, we estimate that a single turbulent patch has a vertical extent of about 40 cm and contains approximately 25 points. Since the features within this turbulent patch are highly chaotic, it is doubtful that the small-scale structure contained within this region were sufficiently resolved.~~

~~While results~~ Results on non-rotating mode-2 ISWs, especially with regards to their mass transport capabilities (Deepwell and Stastna (2016); Salloum et al. (2012); Brandt and Shipley (2014); Terez and Knio (1998)), are readily available ~~, however the case of~~ and there is considerable contact between the experimental and numerical modeling literature. This is exemplified by recent progress on quantifying the effects of displacing the pycnocline center from the mid-depth (Carr et al. (2015); Olsthoorn et al. (2013) In contrast, mode-2 ISWs in a rotating reference frame ~~has only been investigated~~ have been document experimentally by Maxworthy (1983)~~. We extend that research~~ , but no high resolution numerical simulations that provide concrete examples of phenomena future experimental efforts could aim to document exist. We provide such simulations below, with a focus on the ~~breaking of~~ overturning induced by the rotation modified ISW (or Kelvin wave, depending on one's choice of terminology) at the focusing boundary.

Our primary qualitative results that could be confirmed in the laboratory concern the fundamentally three dimensional nature of the shear instability at the edges of the mode-2 wave's core, and the the details of the spatial structure of the span-wise kinetic energy flux. The former could be visualized by a PIV system with a light sheet oriented in the span-wise direction, or along-tank light sheets at varying distances from the focussing wall. The latter could be characterized by the more usual along-tank PIV set up. Moreover, the quantitative results of the Kelvin wave-Poincaré wave resonance and the formation of secondary Kelvin waves in our simulation should provide an easier comparison than field oriented simulations such as those of Sánchez-Garrido and Vlasenko (2009). In terms of the numerical modeling literature, we are interested in exploring how the Schmidt number (or Prandtl number in thermally stratified systems) affects the localized shear instabilities generated near the Kelvin wave crest. This is important since Schmidt numbers representative of salt stratification ($Sc \approx 700$) are presently intractable for numerical simulations on all but the smallest scales, but realistic results may be obtained by choosing a Schmidt number larger than that for a heat stratified system ($Sc \approx 7$) but much smaller than that of salt. It also implies that while field scale simulations like those of Sánchez-Garrido and Vlasenko (2009) may have a similar Rossby number to an experimental study, they cannot have the same viscosity and diffusivity, implying that experimentalists need to carefully assess what aspects of such simulations they may successfully observe in the laboratory.

The remainder of the paper is structured as follows: the set up of the numerical experiments and numerical methods are outlined first, with the results that follow structured to identify fundamental differences between rotating and non-rotating evolution, characterize the three-dimensional structure of near wall overturning, and point out the importance of ~~keeping~~ using a realistic Schmidt number ~~than $Sc = 1$~~other than $\mathrm{Sc} = 1$, which has been consistently used in past literature.

1.1 Configuration of Numerical Experiments

We have run a series of direct numerical simulations (DNS) in a setup similar to that of Maxworthy (1983)~~. These experiments~~ , who employed a gravity intrusion ~~in a rectangular domain~~ from a lock release in a rotating~~reference frame~~ , rectangular tank to generate mode-2 waves. ~~On experimental scales, both the gravity intrusion and the subsequent set of rank-ordered mode-2 internal solitary-like waves are modified by rotation.~~ Since the flow develops from a state of rest the precise definition of the term "Direct Numerical Simulation" from the turbulence literature, namely that grid spacing must be smaller than the Kolmogorov microscale, cannot be directly translated to the present situation. We define DNS in the sense commonly adopted in the stratified flow modeling literature, with Arthur and Fringer (2016) providing a concrete example. These authors state that DNS is a three-dimensional simulation which has a grid spacing which is "within approximately one order of magnitude of the Kolmogorov length scale". The Kolmogorov scale for transitional flows is defined in an ad hoc manner, usually via the explicit calculation of the viscous dissipation rate. The grid scale of our simulations is comparable to this usage since it is within an order of magnitude of the Kolmogorov scale defined from the maximum local dissipation rate. Moreover, our numerical method is spectral in all directions, and hence formally higher order than that used in Arthur and Fringer (2016). The spectral filter used to control aliasing applies only to the largest 30% of wave numbers and leaves the majority untouched, and no subgrid scale model as in Large Eddy Simulation (LES) is used. Based on these considerations, and in the absence of a better term, DNS will be used throughout.

We form the gravity intrusion by releasing a large density perturbation into a quiescent, quasi-two-layer background stratification (~~Figure 1~~ figure 1 shows this so–called lock-release configuration). Algebraically, the density field has the form,

$$\rho(x,z) = \rho_0 - \frac{\Delta\rho}{4}\left[\tanh\left(\frac{z-z_0-\eta(x)}{h}\right) + \tanh\left(\frac{z-z_0+\eta(x)}{h}\right)\right],$$

~~where~~

$$\eta(x) = \frac{H_m}{2}\exp\left[-\left(\frac{x}{L_m}\right)^p\right],$$

$$\rho(x,z) = \rho_0 - \frac{\Delta\rho}{4}\left[\tanh\left(\frac{z-z_0-\eta(x)}{h}\right) + \tanh\left(\frac{z-z_0+\eta(x)}{h}\right)\right], \tag{1}$$

where z_0 is the location of the background pycnocline, h is the half-width of the pycnocline, and,

$$\eta(x) = \frac{H_m}{2}\exp\left[-\left(\frac{x}{L_m}\right)^p\right], \tag{2}$$

describes the perturbation in which H_m, L_m, and p set the height, width, and transition length, respectively. ~~This~~ The above specification of stratification leads to a single hyperbolic tangent profile for $x \gg L_m$ and a double hyperbolic tangent profile with an intermediate density layer for $x \ll L_m$. ~~The~~ As is typical of studies of mode-2 waves (Davis and Acrivos (1967); Stamp and Jacka (the pycnocline is centred ~~on~~ at the mid-depth ~~, while the rest of the~~ ($z_0 = L_z/2$). The stratification parameters are listed in table 1. For comparison, the domain size is ~~6.4 m × 0.4 m × 0.3 m~~ $L_x \times L_y \times L_z = 6.4\ \text{m} \times 0.4\ \text{m} \times 0.3\ \text{m}$.

Table 1. Stratification parameters.

H_m (m)	L_m (m)	p	$\Delta\rho/\rho_0$	z_0 (m)	h (m)
0.1	0.3	8	0.02	0.15	0.02

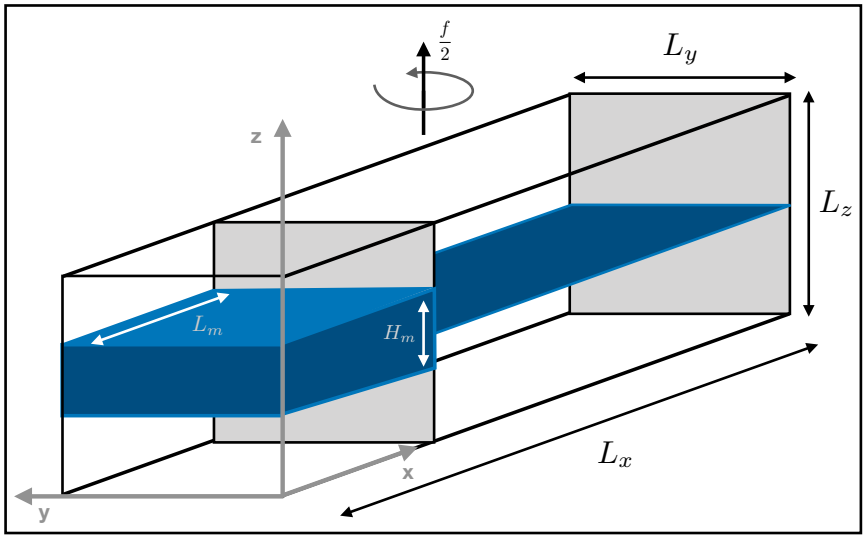

Figure 1. Schematic of the numerical domain. The blue region, centred at the mid-depth, corresponds to $\rho = \rho_0$ with heavier fluid below and lighter fluid above. All lengths have the units of meters and the rotation rate has the units of s^{-1}.

We have completed a suite of numerical simulations at various rotation rates and Schmidt numbers. The rotation rate has been specified using the Coriolis parameter, f, which is defined in the usual way as twice the rotation rate. We define our maximum Coriolis parameter as $f_0 = 0.105\ \text{s}^{-1}$ which is comparable to the literature (Grimshaw et al. (2013)) and~~in particular~~, in particular, to values achievable in the Coriolis Rotating Platform in Grenoble.

~~We characterize the parameters of~~ Following the work of Maxworthy (1983), we characterize the leading wave in regard to ~~their~~ its size at the $y = 0$ m wall. In particular, the wave speed, c_w, and amplitude, a_w, ~~will be~~ are parametrized at this boundary because it is where they reach their maximal values due to the focusing of mass and energy by rotation. The amplitude is defined as the average maximum upstream displacement of the $\rho(z_0 \pm h)$ isopyncals ~~just prior~~ (for a schematic see figure 2 in Deepwell and Stastna (2016)). A representative value (table 2) is chosen just prior (in time)

to the formation of instabilities. The wave speed, measured as the speed of the location of the maximum displacement, is independent of the rotation rate and has a value larger than the linear long wave speed due to the large amplitude nature of these waves. The amplitude is only weakly dependent on the rotation rate or Rossby number. In general, increasing the initial perturbation, both L_m and H_m, leads to the formation of more individual ISWs, larger wave amplitude, and thus higher wave speed. For a comprehensive discussion, consult Deepwell and Stastna (2016); Salloum et al. (2012); Terez and Knio (1998) or Brandt and Shipley (2014) for more details on the relationship between initial tank parameters and the resultant wave. Discussion about how the ISW is formed from the initial conditions will also be deferred to these articles.

The internal Rossby radius of deformation is ~~thus~~ defined as $L_c = c_w/f$, the Rossby number as $\mathrm{Ro} = c_w/fL_m$, the Reynolds number as $\mathrm{Re} = c_w L_m/\nu$, and the Schmidt number as $\mathrm{Sc} = \nu/\kappa$. The kinematic viscosity was $\nu = 2 \times 10^{-6}$ m^2/s for all cases, whereas the mass diffusivity, κ, varied. The parameters and characteristic values for each simulation are presented in table 2. The velocity is scaled by the mode-2, linear, non-rotating, long wave speed, $c_0 = \frac{1}{2}\left(gh\Delta\rho/\rho_0\right)^{1/2}$ (Benjamin (1967)). The average rate of change of the amplitude is given by $a' = -\frac{T}{h}\frac{da_w}{dt}$, where $T = L_m/c_0$ is the characteristic time scale.

Table 2. Case parameters and characterizations.

Case	Sc	f/f_0	c_w/c_0	a_w/h	a'	Re	Ro	L_c (m)
10_0	10	0	1.48	1.47	1.83	6960	∞	∞
10_1/16	10	1/16	1.49	1.45	2.47	7010	23.74	7.12
10_1/4	10	1/4	1.48	1.49	6.02	6960	5.90	1.77
10_1/2	10	1/2	1.46	1.53	6.40	6870	2.91	0.87
10_1	10	1	1.47	1.61	6.76	6900	1.46	0.44
4_0	4	0	1.48	1.46	2.03	6930	∞	∞
4_1/2	4	1/2	1.45	1.53	5.96	6820	2.89	0.87
4_1	4	1	1.46	1.61	6.62	6870	1.45	0.44
1_0	1	0	1.44	1.41	2.88	6770	∞	∞
1_1/2	1	1/2	1.41	1.50	4.97	6640	2.81	0.84
1_1	1	1	1.44	1.61	6.32	6780	1.43	0.43

We briefly contrast our set-up to that of Sánchez-Garrido and Vlasenko (2009). The primary difference is the scale to be ~~modelled~~modeled. While we seek to model laboratory scale motions, and hence resolve both tank scale and small scale motions, in Sánchez-Garrido and Vlasenko (2009) the authors seek to model field scale motions. Hence their ratio of depth to span-wise extent is much smaller than ours. Moreover they model dissipation through an eddy viscosity, while we ~~attempt to~~ carry out a Direct Numerical Simulation (DNS). Nevertheless, the ratio of their Rossby radius to span-wise extent is roughly 0.6, hence similar to some of our experiments. Thus many of the large scale motions in the two sets of simulations can be expected to be similar. In particular, ~~Figure~~ figure 2 of Sánchez-Garrido and Vlasenko (2009) makes for a useful comparison to some of our findings.

1.2 Numerical Methods

~~The governing equations used within our numerical model are the stratified Navier-Stokes equations with the~~ Our numerical model solves the so-called Boussinesq equations of motion on an f-plane ~~and Boussinesq approximations (Kundu et al. (2012)),~~

$$\frac{D\boldsymbol{u}}{Dt} + (-fv, fu, 0) = -\frac{1}{\rho_0}\nabla p + \frac{\rho}{\rho_0}\boldsymbol{g} + \nu\nabla^2\boldsymbol{u},$$

$$\nabla \cdot \boldsymbol{u} = 0,$$

$$\frac{D\rho}{Dt} = \kappa\nabla^2\rho,$$

~~where each variable has~~ (Kundu et al. (2012)),

$$\frac{D\boldsymbol{u}}{Dt} + 2\boldsymbol{\Omega}\times\boldsymbol{u} = -\frac{1}{\rho_0}\nabla p + \frac{\rho}{\rho_0}\boldsymbol{g} + \nu\nabla^2\boldsymbol{u}, \tag{3a}$$

$$\nabla \cdot \boldsymbol{u} = 0, \tag{3b}$$

$$\frac{D\rho}{Dt} = \kappa\nabla^2\rho, \tag{3c}$$

where $\boldsymbol{g}$, the gravitational acceleration vector pointing in the negative z direction, $\boldsymbol{\Omega} = f/2\hat{k}$ is the f-plane rotation vector, and other variables have their usual meaning. ~~The Navier-Stokes~~ These equations are presented in dimensional form, while the remainder of this article will use the following non-dimensionalizations,

$$\widetilde{x} = x/L_m, \quad \widetilde{y} = y/L_y, \quad \widetilde{z} = z/L_z,$$

$$\widetilde{t} = t/T,$$

$$\widetilde{\rho} = (\rho - \rho_0)/\rho_0,$$

$$\widetilde{x} = x/L_m, \quad \widetilde{y} = y/L_y, \quad \widetilde{z} = z/L_z, \tag{4a}$$

$$\widetilde{t} = t/T, \tag{4b}$$

$$\widetilde{\rho} = (\rho - \rho_0)/\rho_0, \tag{4c}$$

where the later is called the density anomaly. Scaling time by the rotation rate is inapplicable because the flow is predominantly a Kelvin wave with a propagation speed independent of the rotation rate. Rather, time has been scaled by $T = L_m/c_0$ since the propagation speed of a Kelvin wave is equivalent to the gravity wave speed in the absence of rotation.

The equations used differ from the oceanic situation in that we take the density as a variable to be evolved, whereas in the ocean it is the salinity and temperature that evolve, with density recovered from an equation of state. The nonlinearity of the equation of state leads to a variety of complex phenomena (e.g. salt fingering, cabbeling, the fact that pure water has a density maximum at 4 degrees Centigrade, etc). In the laboratory, density changes are typically imposed by variations in salinity with the temperature held fixed. Our formulation mirrors this situation, though the experimentally observed diffusivity of salt proves too low for inclusion in the numerical simulations.

Numerical simulations were completed using the Spectral Parallel Incompressible Navier-Stokes Solver (SPINS) (Subich et al. (2013)). SPINS is a psuedo-spectral ~~method uniquely~~ code capable of solving the given problem to a high degree of accuracy in the given geometry. The third-order Adams-Bashforth method with an adaptive time step was used to evolve the flow. Free slip boundary conditions were specified on all walls. This is an unphysical condition compared to the laboratory experiments of Maxworthy (1983), though is standard numerical practice. However, as we will see later, the length scale associated with shear instabilities is much larger than the boundary layer thickness and hence boundary layer effects will not affect the dominant mechanism for shear production. Besides a minor reduction in the energy within the Kelvin wave, we believe that changing to a no slip boundary condition on the side wall will have minimal impact on the Kelvin wave.

The size of the channel and the grid resolution are listed in Table 3. The stated resolution was sufficient for all but two simulations: case 10_1 and case 4_1. These both had the resolutions in the x and z dimensions doubled to have the total number of points be ~~$4096 \times 256 \times 512$~~$N_x \times N_y \times N_z = 4096 \times 256 \times 512$. Grid convergence studies were conducted for these cases because they were the most energetic with the largest and most energetic density overturns. Good agreement was found for the cases with the stated resolution and those with half the resolution. In general, the higher resolutions have been used in this article because of their higher accuracy, though bulk characteristics of the flow computed at the lower resolution remain accurate. For the resolution listed in table 3, the strongly stratified region of the background stratification contains approximately, $2h/\Delta z \approx 33$ points, while the entire stratification has approximately 140 points. Small scale features in the transitional flow typically are a couple centimetres in diameter and contain about 20 points. The applicability of the stated resolution was also found by comparing the grid scale to the Kolmogorov scale which we define using the maximum local energy dissipation rate. In all cases the maximum grid resolution is within an order of magnitude of the Kolmogorov scale. Thus, our simulations are well resolved.

Table 3. Tank dimensions and numerical resolution.

L_x (m)	L_y (m)	L_z (m)	N_x	N_y	N_z	Δx (mm)	Δy (mm)	Δz (mm)
6.4	0.4	0.3	2048	256	256	3.1	1.6	1.2

2 Results: Influence of rotation

We begin by looking at how the ISW is affected by rotation through the Coriolis force. We have chosen the rotation to match that of the Northern Hemisphere which causes objects to be deflected towards the right of their trajectory. In the context of our experiment this leads to span-wise variation in the developing ISW. Maxworthy (1983) found that the wave front became curved as a result of variation of the celerity on wave amplitude. At $\widetilde{y} = 0$ (which we will call the focusing wall) the amplitude and celerity were both larger than at other y values. ~~The time evolution of the scaled, vertically integrated kinetic energy, ξ, for case 10_1 at $t =$ a) $\widetilde{t} = 2.6$ ($t = 25$ s) b) $\widetilde{t} = 5.2$ ($t = 50$ s) c) $\widetilde{t} = 7.8$ ($t = 75$ s) d) $\widetilde{t} = 10.4$ ($t = 100$ s). Colour axis is saturated at early times to show the wave at later intervals.~~

We investigate the location of the ISW crests using the scaled, vertically integrated kinetic energy,

$$\xi(x,y,t) = \frac{\int_0^{L_z} \mathrm{KE}\, dz}{\max_{x,y,t} \int_0^{L_z} \mathrm{KE}\, dz} \tag{5}$$

where the kinetic energy is defined in the usual way, $\mathrm{KE} = \frac{1}{2}\rho_0 \left(u^2 + v^2 + w^2\right)$, and the maximum is over space and time.

The time evolution of ξ displays the bending of the leading internal Kelvin wave and the developing Poincaré waves for case 10_1 (figure 2). Early on (figure 2a), the energy is mostly within the leading wave since insufficient time has passed for radiation to occur. However, at this early time, the wave, which began as a plane wave across the channel, has clearly been affected by the rotation as evidenced by energy being focused towards $\widetilde{y} = 0$. This focusing also resulted in the curvature of the leading Kelvin wave front, a phenomenon which remains evident for the remainder of the simulation.

As time progresses, Poincaré waves form behind the Kelvin wave, as previously described by Sánchez-Garrido and Vlasenko (2009). The Poincaré waves reflect multiple times off both the $\widetilde{y} = 1$ and $\widetilde{y} = 0$ walls. At $\widetilde{t} = 10.4$ ($t = 100$ s) the ratio of total KE on the $\widetilde{y} = 1$ wall to the $\widetilde{y} = 0$ is approximately 0.11 indicating that location of primary activity will be near the focusing wall. The shear also reaches its maximum ~~in this location~~at $\widetilde{y} = 0$, enabling the onset of dynamic instabilities.

The presence of the Kelvin and Poincaré waves in this context is quite common and is dependent on the rotation rate (figure 3). An increasing rotation rate leads to an increase in the angle that the leading wave makes with the normal of the boundary. The Poincaré waves behave similarly as the rotation rate is varied, however they also have the added complication of reflection and non-linear interaction between waves. When rotation is absent (figure 3a), Poincaré waves are unable to form; instead, a simple train of three planar ISWs of decreasing amplitude and energy are formed. Overall, the ~~energy within the Poincaré waves is considerably smaller than the energy in the leading wave , at least over the duration of our numerical experiments.~~ spatial distribution of kinetic energy is dominated by the Kelvin wave front and two secondary features near the focusing wall.

It needs to be mentioned that the presence of side walls removes the possibility of a span-wise invariant geostrophic state forming in the collapse region since the presence of walls enforces that flow is in the along tank direction. This means that the release of mass and energy into the ISWs is greater than when no side wall is present. The detailed dynamics of the near field are interesting, but beyond the present manuscript.

A secondary boundary trapped wave also forms in the rotation modified cases (figure 3b-d). The generation mechanism for this wave is fundamentally distinct from the formation of trailing ISWs in the non-rotating case. In discussing this difference,

ISW will be used to describe the non-rotating waves only, while Kelvin and Poincaré waves will naturally be understood to relate to the rotation modified waves. To see how this secondary Kelvin wave is formed, figure 4 compares the span-wise average ξ of the non-rotating case (case 10_0, in red) to that of the full ξ for case 10_1 (black pseudocolour). At the early time, $\widetilde{t} = 4.7$ ($t = 45$ s), there is a single leading Kelvin wave and a few radiating Poincaré waves which are just beginning to reflect off the $\widetilde{y} = 1$ wall. ~~Scaled, vertically integrated kinetic energy, ξ, for case 10_1 at $t =$ a) $\widetilde{t} = 4.7$ ($t = 45$ s) b) $\widetilde{t} = 6.3$ ($t = 60$ s) c) $\widetilde{t} = 7.8$ ($t = 75$ s). Scaling and colour axis is identical to figure 2. The red plots are the span-wise average ξ profiles for the non-rotating case (Case 10_0), with corresponding maxima locations (vertical lines).~~ The trailing ISWs of the non-rotating case are completely unrelated to the energy distribution of the rotating case. This is clearly evident in figure 4 b) and c) where the second trailing ISW is located where very little energy exists in the rotating case. The third ISW is near where the second Kelvin wave is forming, but this happens to be a coincidence of the choice of the presented time. Later, at $\widetilde{t} = 10.4$ ($t = 100$ s) (figure 3) the third ISW is well behind the second Kelvin wave.

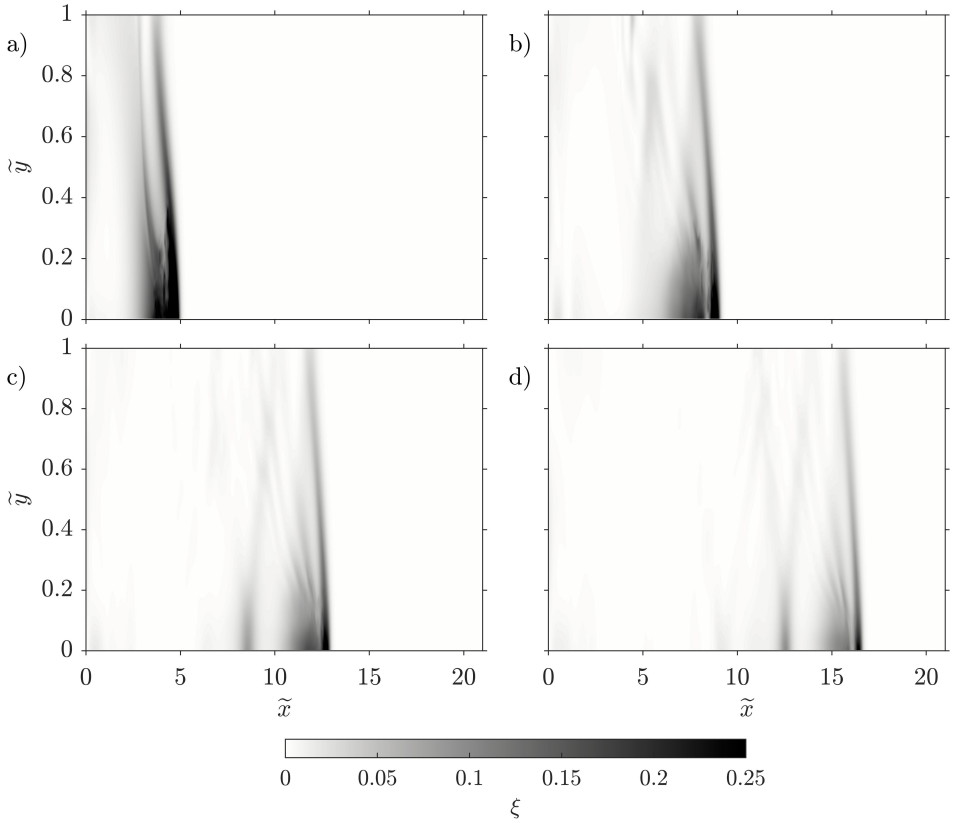

Figure 2. The time evolution of the scaled, vertically integrated kinetic energy, ξ, for case 10_1 at a) $\widetilde{t} = 2.6$ ($t = 25$ s) b) $\widetilde{t} = 5.2$ ($t = 50$ s) c) $\widetilde{t} = 7.8$ ($t = 75$ s) d) $\widetilde{t} = 10.4$ ($t = 100$ s). Colour axis is saturated at early times to show the wave at later intervals.

More importantly, at high rotation rates the second Kelvin wave is clearly formed by a resonance with the Poincaré waves at the focused wall, which is directly contrary to how the trailing ISWs form without rotation (they are the excess mass that isn't trapped by the leading wave). This description appears to be valid for rotation rates greater than $f/f_0 = 1/4$, ~~since~~ while rates slower than this show ~~that~~ the trailing Kelvin wave ~~matches~~ to match the generation of a trailing ISW in the non-rotating case with additional perturbations due to weak Poincaré waves. Renouard et al. (1987) describes Poincaré waves being resonantly generated along the side wall while Melville et al. (1989) clearly shows that the curvature of the wave front is due to the combination of a Poincare and Kelvin wave. Our results are in agreement with both of these results, but now applying to mode-2 ISWs.

As described by Sánchez-Garrido and Vlasenko (2009) the Poincaré waves will continue to remove energy from the leading Kelvin wave, which is then deposited in this secondary Kelvin wave. This deposition primarily occurs on the focusing wall, as opposed to equal deposition on both sides of the channel, because of the broken symmetry caused by the collapse of

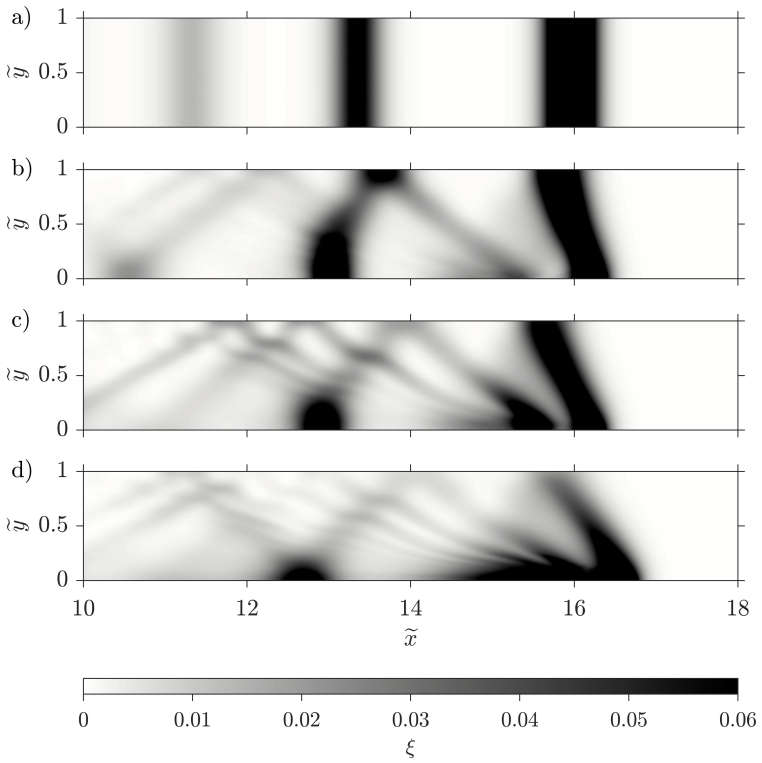

Figure 3. Scaled, vertically integrated kinetic energy, ξ, at $\widetilde{t} = 10.4$ ($t = 100$ s) for case with ~~$f/f_0 =$~~ a) ~~0~~ $f/f_0 = 0$ (Ro$=\infty$) b) ~~1/4~~ $f/f_0 = 1/4$ (Ro$= 5.9$) c) ~~1/2~~ $f/f_0 = 1/2$ (Ro$= 2.91$) d) ~~1.~~ $f/f_0 = 1$ (Ro$= 1.46$). The scaling is by the maximum over the $f = f_0$ case and the colour axis is saturated to emphasize the Poincaré waves emanating from the focusing region and their reflection off the $\widetilde{y} = 1$ wall. The maximum of the unscaled ξ for each case is a) 0.08 J·m b) 0.12 J·m c) 0.16 J·m d) 0.27 J·m.Though in non-dimensional form, the axes have correct dimensional scaling.

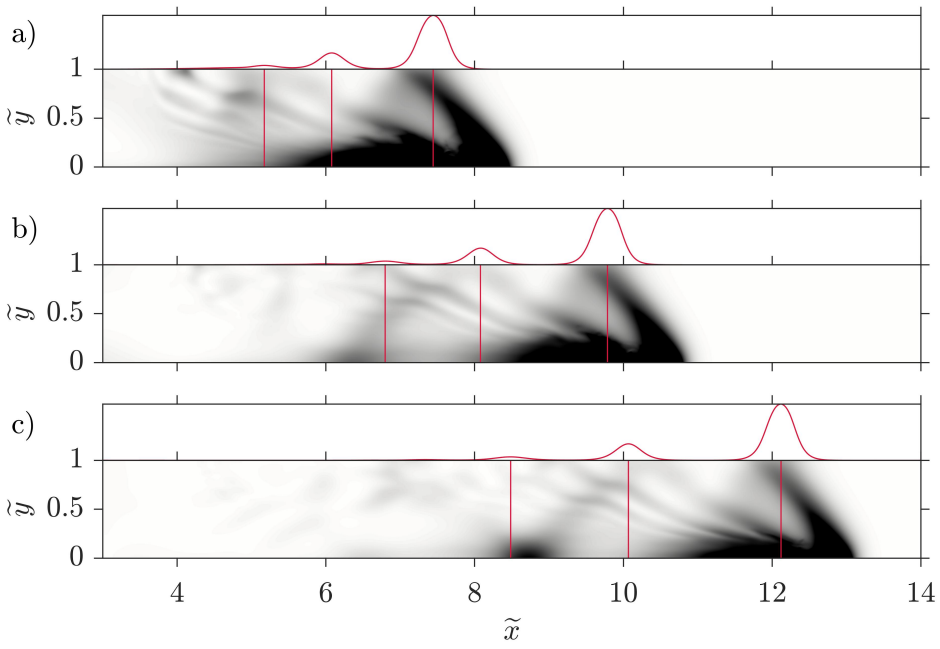

Figure 4. Scaled, vertically integrated kinetic energy, ξ, for case 10_1 at $t = $ a) $\widetilde{t} = 4.7$ ($t = 45$ s) b) $\widetilde{t} = 6.3$ ($t = 60$ s) c) $\widetilde{t} = 7.8$ ($t = 75$ s). Scaling and colour axis is identical to figure 2. The red plots are the span-wise average ξ profiles for the non-rotating case (Case 10_0), with corresponding maxima locations (vertical lines).

intermediate fluid on one end of the channel. This means that there is more residual kinetic energy at $\widetilde{y} = 0$ (compared to $\widetilde{y} = 1$), and that the time for the Poincaré wave to resonantly interact with the Kelvin wave is greater at $\widetilde{y} = 0$ since both are traveling in the same direction. Once the secondary Kelvin wave is fully developed, this resonance can be considered analogous to a Mach stem in that the energy builds up on the boundary enough that the reflection no longer occurs at the boundary, and moves instead some distance away from the wall.

As energy is drained from the leading Kelvin wave and deposited into the secondary wave, the secondary wave will eventually become more energetic than the first resulting in an eventual overtaking. Our simulations do not show this feature since our channel is not long enough and we are focused on the shorter time scales associated with the energetics of the leading Kelvin wave. See Sánchez-Garrido and Vlasenko (2009) for a description of overtaking. Unfortunately, we predict that the overtaking is likely to remain undetected in a laboratory experiment with rectangular geometry because of the considerable time, and thus length of channel, required for the energy transfer to occur.

The differentiation of whether a wave is a Kelvin wave or a Poincaré wave is made difficult because of the non-linearity associated with the large amplitude of these waves. The classical linear theory~~presented by Kelvin~~, as presented in standard textbooks (Vallis (2006); Kundu et al. (2012)) describes a Kelvin wave as one which has no span-wise velocity, and where the wave crest does not curve in the span-wise direction. A simple check shows that the leading and radiating waves have significant span-wise velocities which would indicate that they are not Kelvin waves (in the classical sense). However, we choose to label

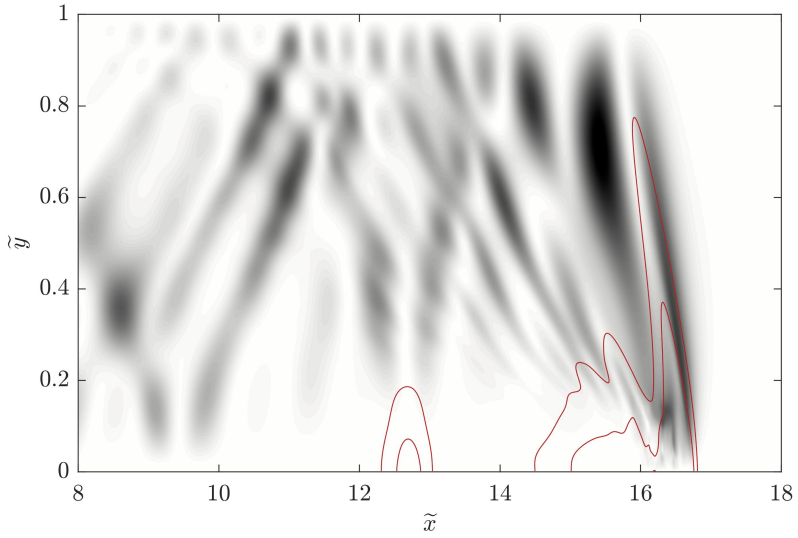

Figure 5. Vertically integrated v^2 at $\widetilde{t} = 10.4$ ($t = 100$ s) for case 10_1. Red contours are level curves of the vertically integrated KE.

the radiating waves as Poincaré waves and the leading wave as a Kelvin wave because both fit all other descriptions of the particular wave type.

We just saw that the radiating Poincaré waves resonate to form a secondary Kelvin wave. Since this secondary wave is separated from the chaotic leading wave, it could possibly fit better in the description of a classical Kelvin wave. Figure 5 presents a test for this by plotting the vertically integrated span-wise squared velocity (in dark) and contours of the total vertically integrated KE (in red). The secondary wave (at $\widetilde{x} \approx 12.5$) does indeed show no span-wise velocity or wave crest curvature, and thus our description of it as a Kelvin wave is valid. We also notice that the region directly trailing the wave also has little to no span-wise velocity. Looking back at figure 3b and c it becomes clear that there are Kelvin waves directly trailing the leading wave at weaker rotation rates (the highest rotation rate requires more time to settle into this description). This Kelvin wave is distinct from the previously described secondary wave. In this case they are formed out of the remains of the excess focused mass along $\widetilde{y} = 0$. To distinguish this Kelvin wave from the leading wave, we call it the Kelvin wave tail.

The dynamics seen thus far are fundamentally different than in the case without the side walls. As described in Coutino and Stastna (2017), without the walls the Poincaré waves steepen and eventually breakdown into a non-linear wave packet as dispersive effects take over. The addition of side walls appears to slow the large-scale breakdown of the leading wave. Rather, this energy is moved towards the side wall, and is then radiated leeward into trailing Poincaré waves at a slower pace.

The advection of kinetic energy within the Kelvin and Poincaré waves is key to understanding how the distribution of this energy is influenced by the side wall. The span-wise flux of KE (figure 6) reveals some interesting features. Of primary interest is that the leading Kelvin wave ~~which has~~ induces both positive and negative span-wise flux of KE. Close to the wall (figure 6c), the front of the wave has advection away from the wall, which then becomes a stronger, more localized ~~,~~ return of kinetic

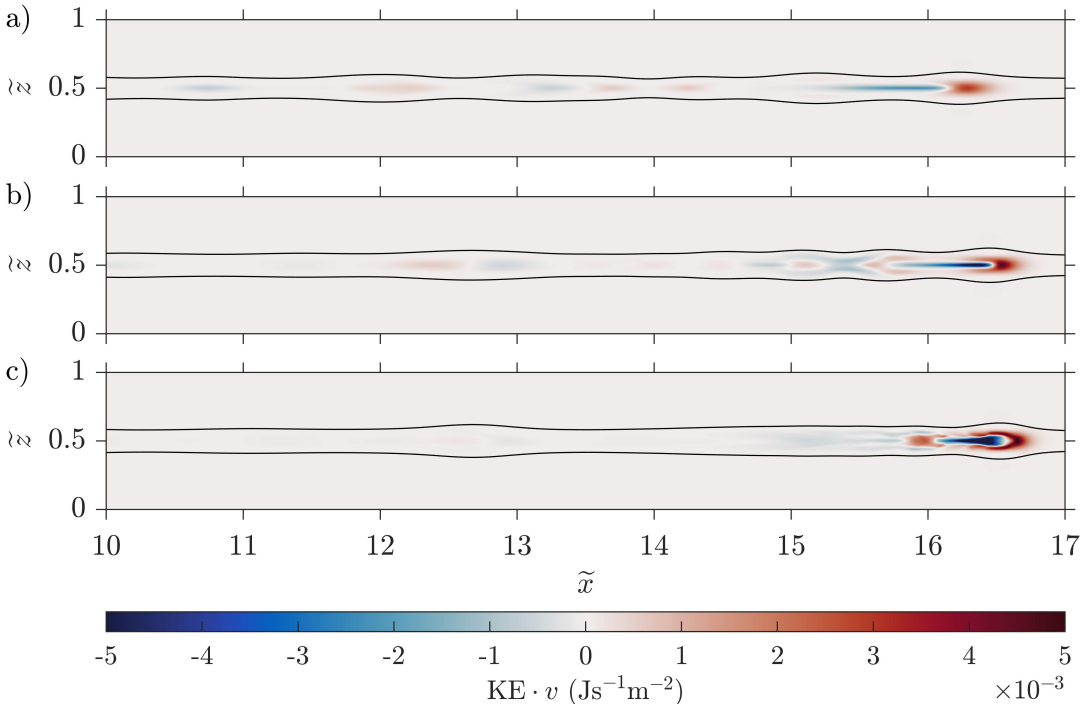

Figure 6. Span-wise kinetic energy flux density for case 10_1 at $\widetilde{t} = 10.4$ ($t = 100$ s) and $\widetilde{y}$ = a) 1/2 b) 1/4 c) 1/8.

energy flux towards the wall within the downstream portion of the leading wave. Further from the side-wall (figure 6a), the KE flux is weaker by nearly an order of magnitude and the structure has changed so that the leading wave contains more positive flux.

The secondary Kelvin wave (near $\widetilde{x} = 12.75$ m) has much weaker KE flux even though the waves are of comparable amplitude. The leading wave still contains residual energy from the K-H instabilities while the secondary wave receives energy from upstream. To within 3%, the same KE flux is advected towards and away from the focusing wall in this secondary Kelvin wave.

For comparison purposes, we have completed the same simulation in two dimensions while allowing transverse flow to be coupled to horizontal motion through the Coriolis force (i.e. a two-and-a-half dimensional model). Since there exists no side wall, the radiated ISWs are smaller because much of the energy remains within the geostrophic state. Regardless of the waves being smaller and thus traveling slower, the KE flux in the leading wave of the 2D case (not shown) is different from that of the 3D case with sidewalls, especially near the wall. Further from the side walls, the two become more similar yet remain distinct in the magnitudes and distributions of the KE flux.

The span-wise variation in the KE flux along the mid-depth ($\widetilde{z} = 0.5$ m) ~~further describes~~ provides a different way to visualize the KE flux away and towards the focusing wall. Figure 7 displays both the magnitude of the flux (colour) and direction (streamlines with flow going from right to left) in a reference frame moving with the wave. The strongest KE flux is directed

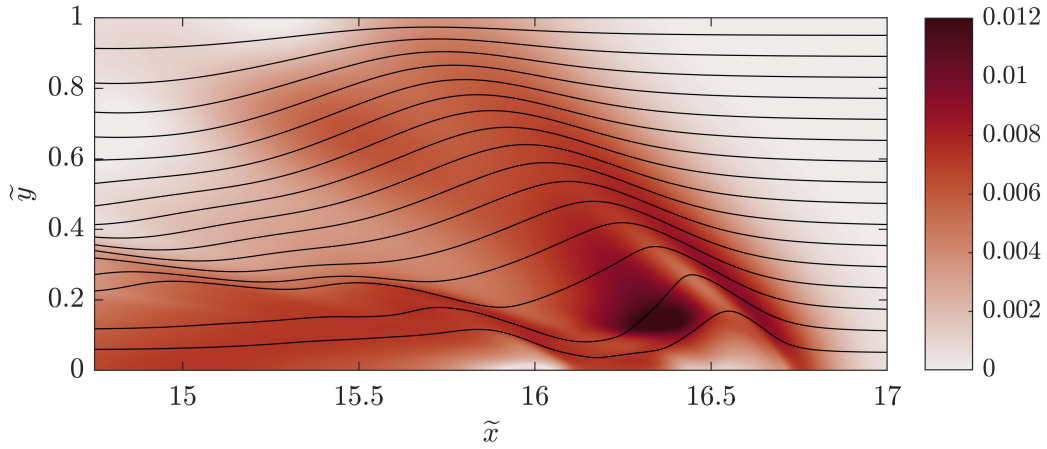

Figure 7. Horizontal kinetic energy flux density for case 10_1 at $\widetilde{t} = 10.4$ ($t = 100$ s) and $\widetilde{z} = 0.5$. Streamlines show direction of KE flux in reference frame moving with the leading wave (i.e. flow is right to left). Colour axis shows magnitude of KE flux.

towards the wall in the aft of the Kelvin wave. We hypothesize that this KE flux is the cause of wave breaking in the Kelvin wave (the details of which we present in the next section). The kinetic energy near the wall then leaves the Kelvin wave and travels along the wall until forming the Kelvin wave tail some time later.

3 Results: Details of wave breaking

Now that the description of the global wave field has been presented, we move onto the localized behaviour of the leading Kelvin wave at the focusing wall. As described by Maxworthy (1983), the dominant instability takes the form of a pair of Kelvin-Helmholtz (K-H) billows at the crests of the leading Kelvin wave at the upper and lower extrema of the wave (figure 8a), ~~and~~ or, alternatively, at the edges of the pycnocline.

In the highest rotation rate (case 10_1) the instability is confined to within approximately ten centimetres (a quarter of the channel width) of the focusing wall (figure 8b-d). As the rotation rate decreases, the extent of the instability decreases. Table 4 lists the length scale, l^*, of the initial billow and the non-dimensional duration of the shear instability, t^*. Except in case 10_1, the instabilities stop within the duration of the simulation. For case_1 the size of the K-H billows decreases significantly near the end of the simulation. It is worth repeating that higher rotation rates (smaller Rossby numbers) lead to larger and longer lasting shear instabilities within the crests of the Kelvin wave.

For all cases, the Kelvin-Helmholtz billows simultaneously form as pairs with a vortex above and below the pycnocline. Furthermore, except during the early energetic K-H formation, these billows remain synchronous even during the process of being broken down. ~~For a while it appeared as though case 10_1 made a transition from simultaneous~~ Comparison to the observations of Moum et al. (2003) is evident as upstream isopycnals are compressed along the wave crest followed by the K-H ~~formation to an oscillatory one. However, this transition disappeared when the resolution was increased to properly resolve~~

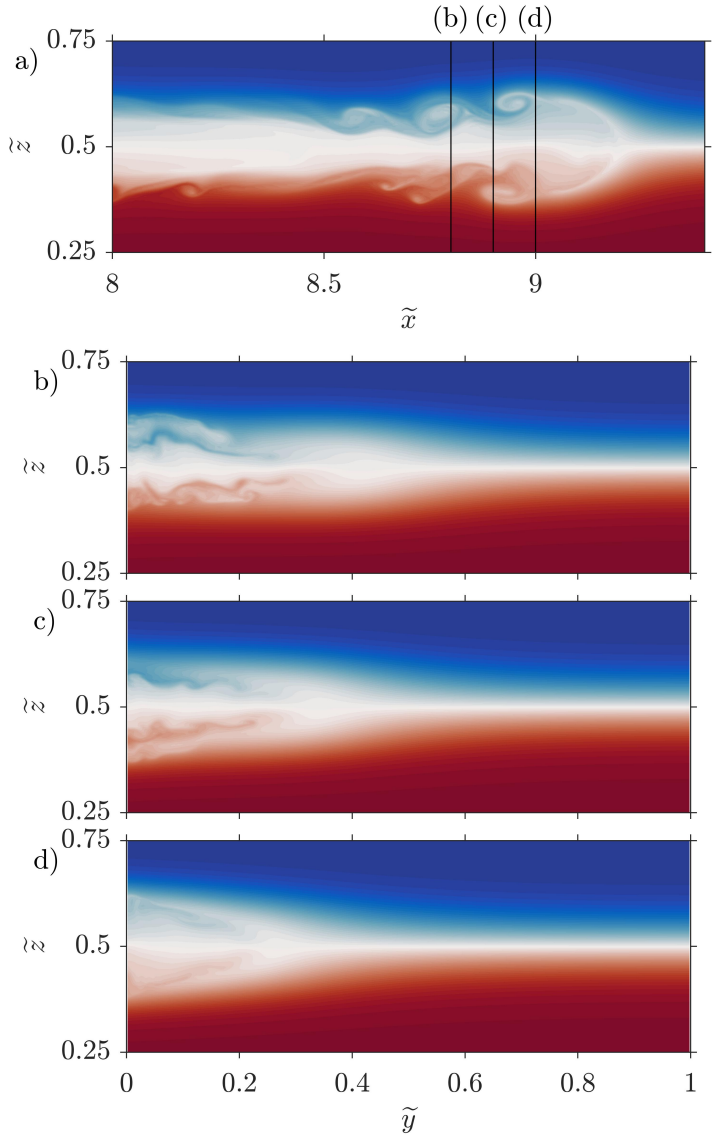

Figure 8. Density anomaly, $\widetilde{\rho}$, at $\widetilde{t} = 5.2$ ($t = 50$ s) and a) $\widetilde{y} = 0$ b) $\widetilde{x} = 8.8$ c) $\widetilde{x} = 8.9$ d) $\widetilde{x} = 9$ for case 10_1.

~~this case. Whether the vortices form simultaneously or not, they are visually analogous to a von Karman vortex street. We note that there is no quantitative correspondence since the object~~ billows. These K-H billows can also be considered analogous to a von Karman vortex street. In a reference frame moving with the wave, the background flow is directed around the wave, much like it is around a cylinder in von Karman's classical experiment. The analogy is limited since the Kelvin wave core is not a solid, ~~there are no boundary layers, and the rotation rate is an additional parameter which affects the form of the vortex street.~~

Table 4. ~~Density anomaly, $\widetilde{\rho}$, at $\widetilde{t} = 5.2$ ($t = 50$ s)~~ Length and ~~a) $\widetilde{y} = 0$ b) $\widetilde{x} = 8.8$ c) $\widetilde{x} = 8.9$ d) $\widetilde{x} = 9$ for case~~ time scales associated with localized shear instabilities.

Case	l^* (m)	t^*
10_~~1.~~0	0	0
10_1/16	0.02	1.35
10_1/4	0.05	1.88
10_1/2	0.07	7.93
10_1	0.10	>12

and the core bends backward away from the wall due to the rotation (and hence isn't a cylinder). Moreover, the instability is a shear instability, as opposed to a boundary layer separation.

At the wave crest, the wave has the expected exponential decay (figure 8d). Further behind, a description that is purely in the $\widetilde{x} - \widetilde{z}$ plane is no longer valid ~~,~~since the wave front curves backwards, as discussed in the previous section. However, the instabilities remain trapped along the side wall (figure 8b and c), while the wave itself, which created the instabilities, remains stable further away. In the density field, the instabilities are recognized as interleaving layers of lighter and denser fluid associated with the roll-up of the K-H billows. The span-wise extent remains largely unchanged as the vortices leave the leading wave. This means that rotation causes mixing and turbulence to occur at a preferred location, namely on the focusing wall. Should the geometry, or environmental forcing (e.g. flow over a sill in a fjord) cause Kelvin waves to be generated at a specific location, this would indicate that one side of the channel would experience more mixing. The aforementioned fjords, as well as narrow lakes would be particularly susceptible to this.

We find that changes in the rotation rate (i.e. the strength of the Coriolis force) influence the intensity of the K-H billows (figure 9). Though the initial available energy is the same in all cases, the higher rotation rates lead to higher localized kinetic energy density. At early times (first column of figure 9) the amplitude of the leading waves are all comparable, but have varying levels of stability. The cases with increasing rotation are far more energetic. Fundamentally, these vortices are formed from stratified shear instabilities commonly associated with larger amplitude waves (Brandt and Shipley (2014)). This leads us to suggest that a coastally trapped ~~wave~~ ISW has a lower minimum amplitude threshold for instability generation ~~. Over time this causes the wave to reduce in amplitude considerably faster than would be the case without the presence of rotation~~compared to a ISW away from boundaries. The precise reason for the lower minimum amplitude remains an open problem, but it likely has to do with the mass and energy flux towards the focusing region discussed in the previous section.

As time progresses, the wave sheds energy and mass in the shear instabilities until reaching a critical amplitude, after which the wave remains stable, but continues to decay because of the lossy behaviour of the core region of large amplitude mode-2 ISWs (Deepwell and Stastna (2016)). At $\widetilde{t} = 10.4$ ($t = 100$ s), only the highest rotation rate still produces shear instabilities. In comparison, the non-rotating case is laminar and time-invariant, apart from small dissipative effects for all times. The weaker rotation rate cases do not exhibit instabilities at later times, but rather the mass from the shed vortices has formed the Kelvin

wave tail. This wave is also immediately apparent from figure 3 which shows the kinetic energy within this wave directly behind the leading Kelvin wave. Over time the lower rotation rates show that this Kelvin wave tail obtains energy from the leading wave and ~~eventually overtakes~~ will eventually overtake it. At the highest rotation rate, the shear instability remains active for the entire simulation which makes it difficult for ~~this wave~~ the Kelvin wave tail to form.

The emergence of shear instabilities is correlated with the rotation rate. That is, a higher rotation rate is associated with an earlier shear instability. The higher rotation causes greater fluid to be directed towards the focusing wall which leads to a greater initial amplitude which creates favourable conditions for shear instabilities. Though the initial amplitude is correlated with rotation rate (figure 10), the three fastest rotations result in similar wave amplitudes as the experiment continues. This leads to the interesting question of whether Kelvin waves have a stability restriction based on their amplitudes, though the form of their creation here (as a collapse of a span-wise invariant perturbation) greatly impacts the dynamics, especially with the

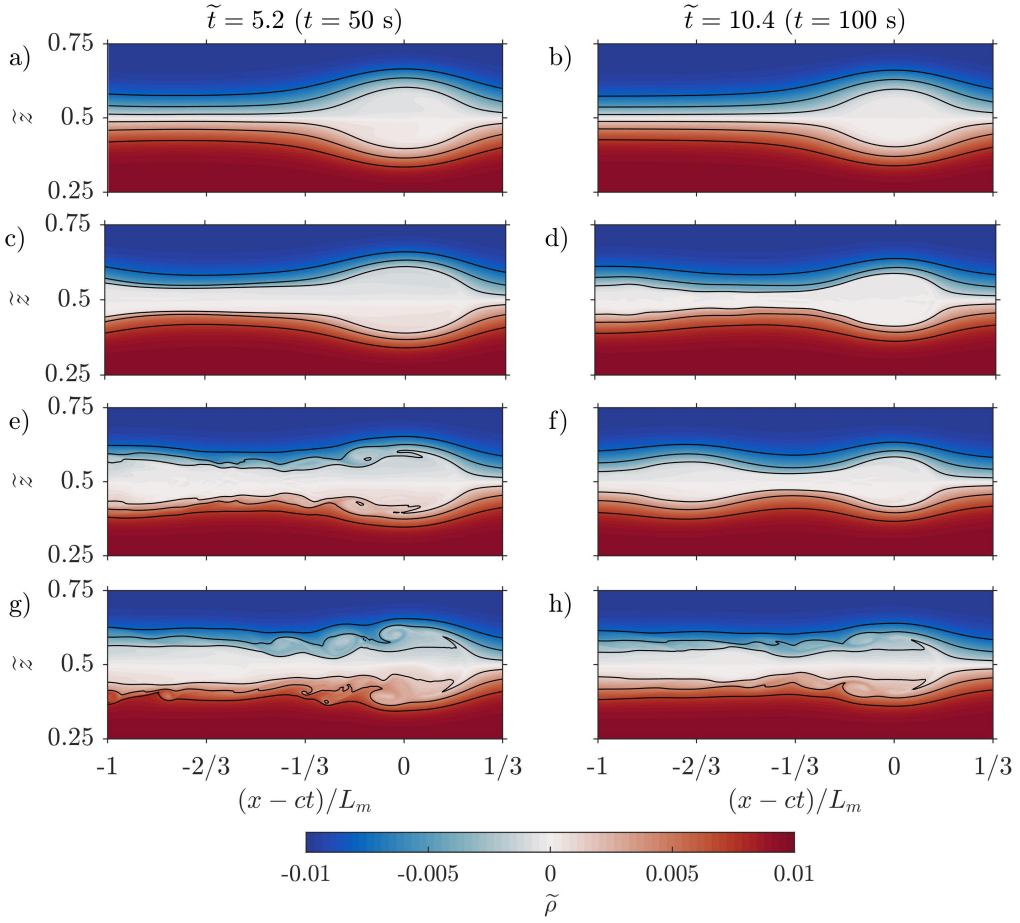

Figure 9. Density anomaly, $\widetilde{\rho}$, at $\widetilde{y} = 0$ for $f/f_0 =$ a,b) 0 c,d) 1/4 e,f) 1/2 g,h) 1. Black contours are equispaced isopycnals between $\rho(z_0 - h)$ and $\rho(z_0 + h)$. All cases have ~~$Sc = 10$~~Sc = 10.

K-H billows. Though the Richardson number is not applicable in the upper and lower layers where there is no vertical density variation, within the wave core the Richardson number drops below 1/4 around the edge of the mode-2 bulge while the K-H billows form.

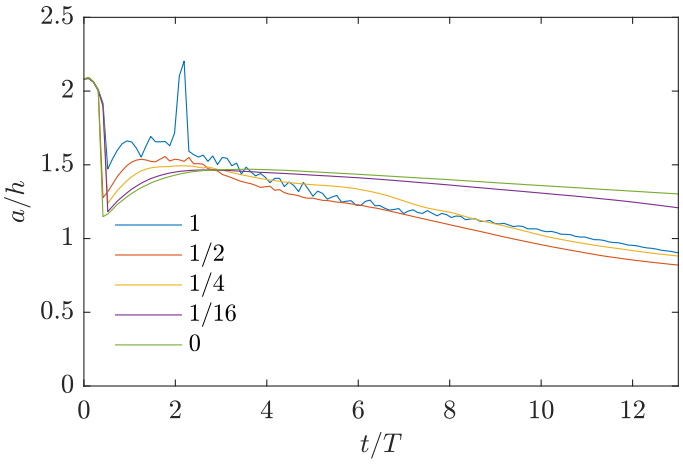

Figure 10. Wave amplitude as a function of time for different rotation rates (f/f_0 in legend). All cases have ~~$Sc = 10$~~Sc $= 10$.

The wave amplitude decay rate, $a' = -\frac{T}{h}\frac{da_w}{dt}$, increases with rotation rate (table 2, and figure 10). At larger rotation rates this is a result of a greater initial amplitude, while slower rates create far less K-H billows and the associated loss of mass. At $\widetilde{t} = 5.2$ ($t = 50$ s), the kinetic energy within the leading wave increases with rotation rate (first column of figure 11). The kinetic energy also becomes localized in space at the K-H billows. At later times, The kinetic energy has decreased most substantially in the higher rotation rates because of the shear instabilities.

Figure 12 shows the kinetic energy slices in the $\tilde{y} - \tilde{z}$ plane at the crest of the Kelvin wave (ISW in the non-rotating case). The case of no rotation has an essentially span-wise invariant wave front, whereas the rotation breaks the symmetry by curving the wave front. Along the cross-section of maximum amplitude this appears as an exponential decay of the wave amplitude. Essentially all of the kinetic energy resides within the characteristic isopycnals, $\rho(z_0 \pm h)$. Furthermore, the density overturns resulting from the instabilities are correlated with the locations of maximum KE.

Over time, due to the radiation of energy into trailing waves, the leading Kelvin wave reduces in amplitude, span-wise width, and KE. The time dependent nature of the width, and thus the exponential decay, results in an increased localization of KE along the focusing wall (seen very clearly in the second row of figure 12). This is true along the cross-section of maximum amplitude where the decaying Kelvin wave applies. In the curved portion of the leading wave, this coincides with a simple reduction of the width of the curved wavefront.

Maxworthy (1983) found that the measured Rossby radius of deformation, L_M, (that is, the distance from the wall for the amplitude to drop by a factor of e) was a factor of two smaller than the calculated Rossby radius, L_c. Only the highest rotation rate has L_M smaller than the width of the channel for us to make a comparison. Case 10_1 has the factor being close to 2.6,

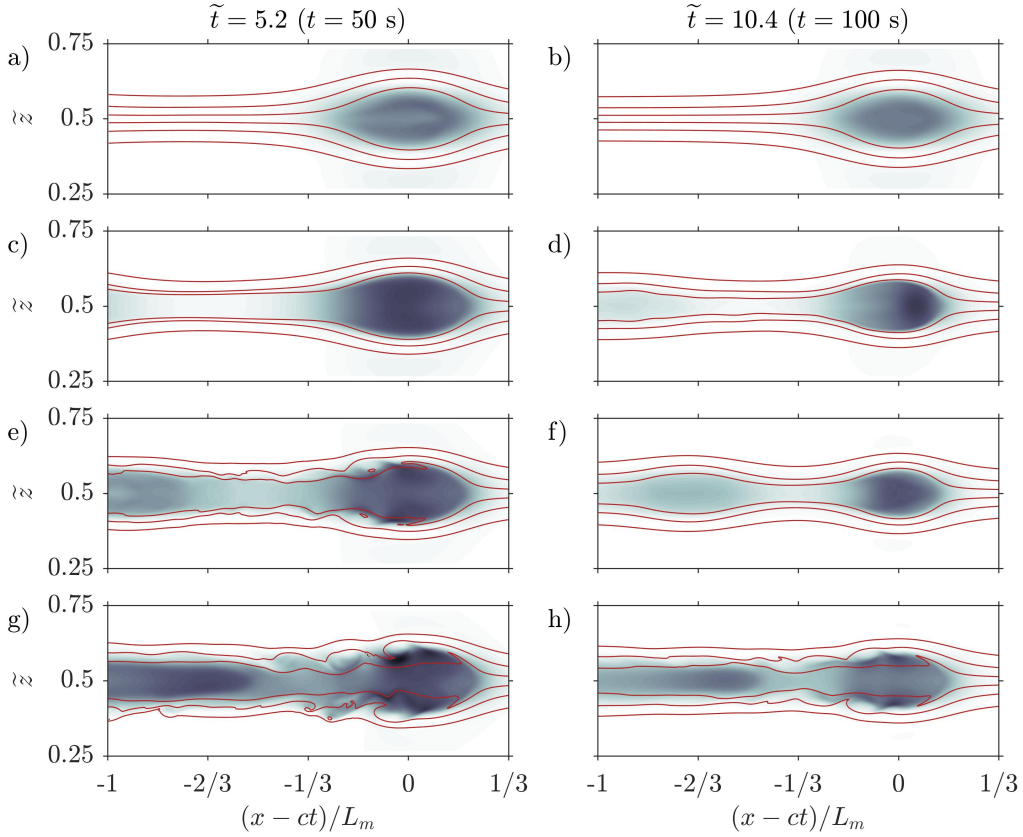

Figure 11. Kinetic energy density at at $\widetilde{y} = 0$ for $f/f_0 =$ a,b) 0 c,d) 1/2 e,f) 1. Red contours are the same as in figure 9. All cases have ~~$Sc = 10$~~Sc $= 10$.

which is comparable. This does not appear to be the case at lower rotation rates since these cases have their amplitudes decay over the entire channel width even though the Rossby radius ~~increase~~ increases by up to a factor for 4. This could be due to the narrowness of the channel compared to the Rossby radius or more likely a difference in measurement technique. Maxworthy (1983) made ~~their~~ his estimate based on the projection of the wave field onto the $\widetilde{y} - \widetilde{z}$ plane. This would lead to a weaker decay rate since the wave curves backwards away from the cross-section with a fixed $\tilde{x}$ at which our estimate is made. In other words the method of Maxworthy (1983) integrates in the along tank direction, while we choose a particular stream-wise location for our estimate. The width of the channel will, however, adjust the reflection of the Poincare waves and thus the resonance of the secondary Kelvin wave, but this will have no impact on the leading wave.

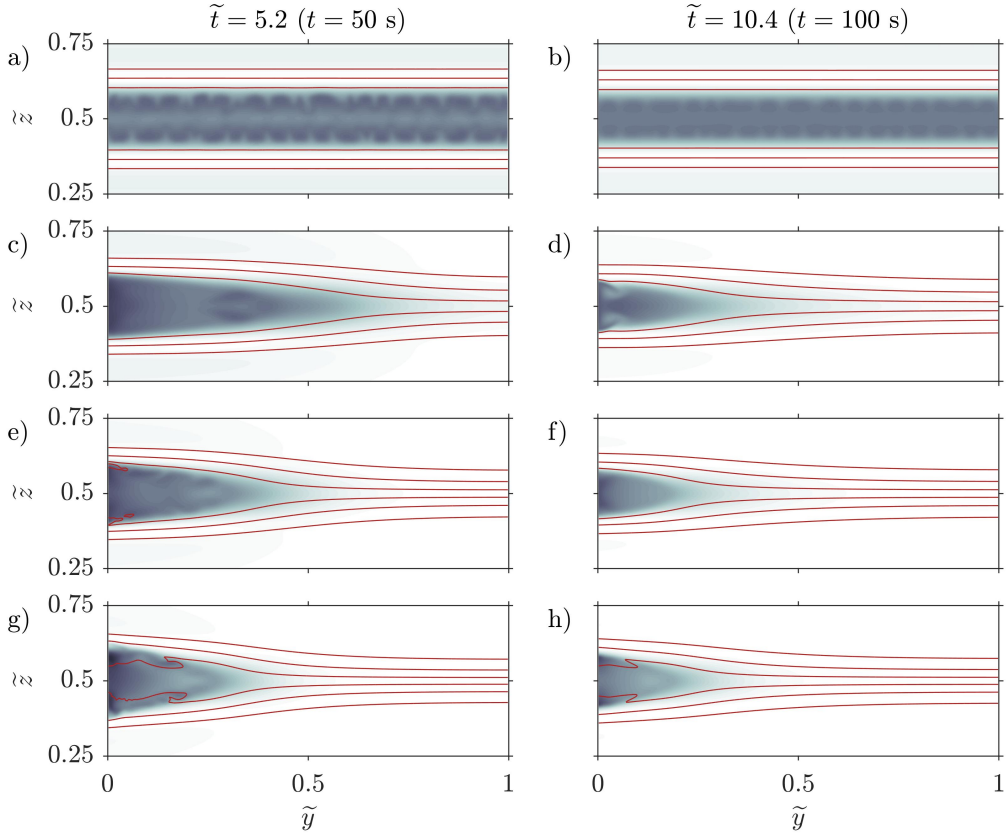

Figure 12. Kinetic energy density at the location of maximum amplitude for $f/f_0 =$ a,b) 0 c,d) 1/4 e,f) 1/2 g,h) 1. Red contours are the same as in figure 9. All cases have ~~$Sc = 10$~~Sc $= 10$.

4 Results: Schmidt number dependence

The shear instabilities and associated dynamics are fundamentally small scale behaviour which are damped by viscosity and smeared by diffusion, both of which are determined by the properties of the fluid, namely the molecular diffusivity and the viscosity. Experimentally, the diffusivity is fixed by the choice of stratifying solute. Physical values of a salt stratified experiment, which are typical for experiments of this type, give a Schmidt number of approximately 700. Since direct numerical simulations at these values are unattainable due to the resolution required, we provide here a short description of the impact that various Schmidt numbers have on the results presented thus far. Of importance is measuring the change in the shear instabilities by varying the Schmidt number.

For longer simulations, such as the ones conducted here, the pycnocline will diffuse causing the waves to propagate in a slightly different stratification near the end of the simulation compared to the beginning. Smaller Schmidt numbers have

greater diffusion causing a greater impact (figure 13a). The $\mathrm{Sc} = 1$ case had the pycnocline grow by 70% while the $\mathrm{Sc} = 10$ case only grew by 10%. The background stratification at the end of the experiment is noticeably different (figure 13b).

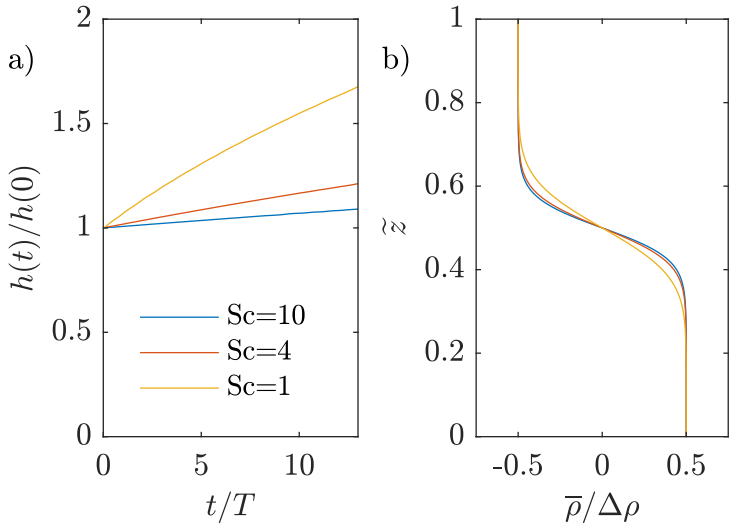

Figure 13. a) Pycnocline half-width as a function of time for different Schmidt numbers. b) The background stratification at ~~$t/T = 12.5$ ($t = 120$ s)~~$\widetilde{t} = 12.5$ ($t = 120$ s).

We find that the wave amplitude is unaffected when compared at various Schmidt numbers. ~~The~~ Thus, the general features characterizing the wave are ~~thus~~ fairly similar at $\widetilde{t} = 5.2$ ($t = 50$ s) (figure 14). The details, however, are significant enough to warrant comment. All Schmidt numbers experience the shedding of Kelvin-Helmholtz billows, but in the lowest Schmidt number case formation ceases at around $\widetilde{t} = 11.7$ ($t = 112$ s) while the other two cases ~~never stop. Since the stratification has broadened in this case , the Richardson number has increased leaving the unstable region for shear instabilities to form.~~ create billows for the duration of the simulation. The higher diffusivity in the $\mathrm{Sc} = 1$ case acts to hinder the production of shear instabilities by quickly diffusing them as they form.

The span-wise profile of the wave also shows the difference (right column of figure 14). The highest Schmidt number case has overturning which is not present in the lowest Schmidt number case. These features are secondary to the over-all behaviour. For example, the total kinetic energy is comparable between all cases at a given rotation rate but remains consistently weaker for lower Schmidt number. The greatest separation between the Sc=1 and Sc=10 case is 13%. As this ratio is only expected to grow as Sc increases, the difference between typical simulations of Sc=1 ~~or Sc=7~~ are bound to misrepresent the smaller dynamical features of an equivalent physical experiment ~~.~~ which is typically salt stratified with a Schmidt number around 700. As a result of this, the dynamics of a physical experiment will look like figure 14a,b with substantially finer details. A thermally stratified experiment, however, will be well represented by figure 14a,b. We are unaware of any experimental work on mode-2 internal waves with stratification achieved by varying temperature.

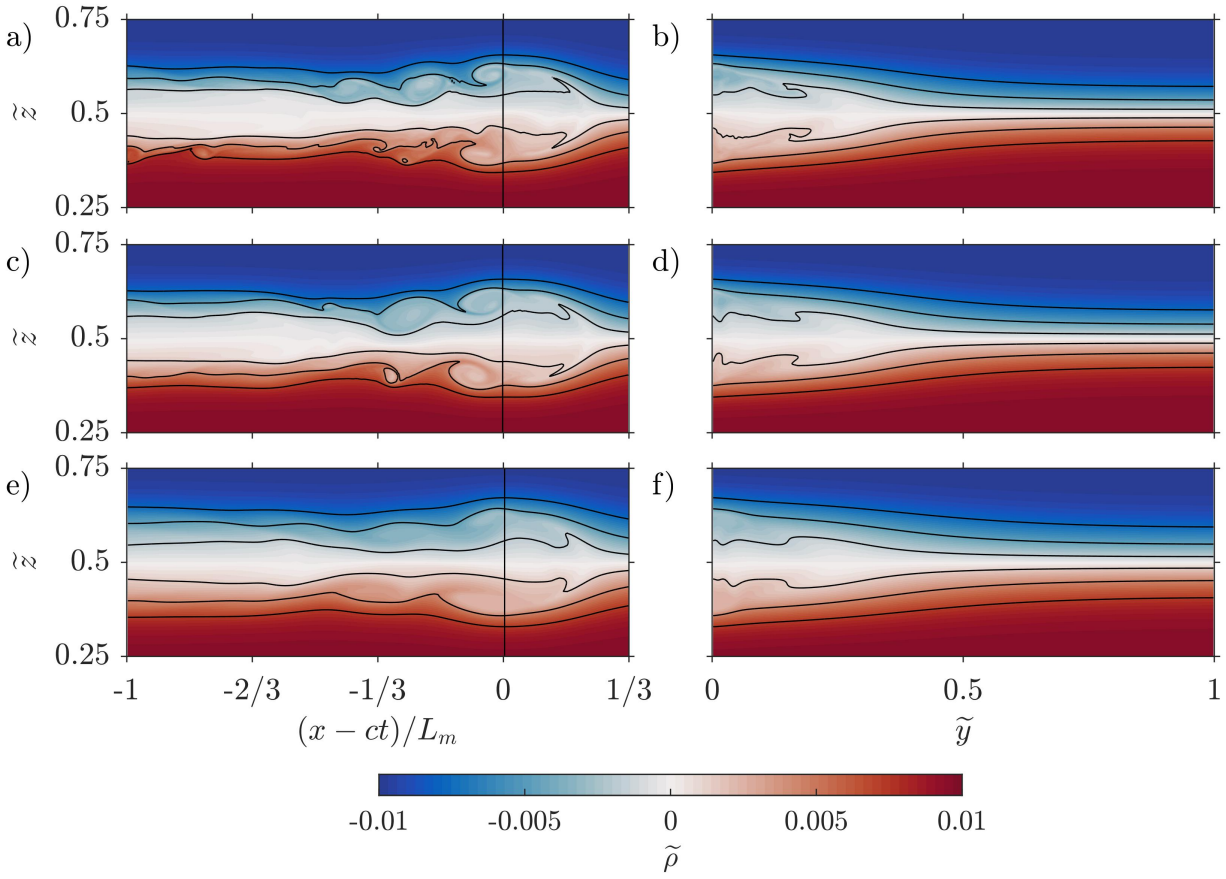

Figure 14. Density anomaly, $\widetilde{\rho}$, at $\widetilde{t} = 5.2$ ($t = 50$ s) with cross-sections at $\widetilde{y} = 0$ (first column) and at the location of maximum amplitude (second column) for Sc = a,b) 10 c,d) 4 e,f) 1. Black contours are the same as in 9. Vertical, black line denotes location of the cross-section shown in the right column. All cases have $f/f_0 = 1$.

In the $f/f_0 = 1/2$ rotation rate cases (comparison not shown) the differences are more obvious. The density field does not clearly show the Kelvin wave tail in the Sc=1 case. Rather, the wave is of such small amplitude that it is nearly indistinguishable compared to the pycnocline width. Only by looking at the vertically integrated KE does the wave appear, but is of considerably smaller magnitude. The fanning structure seen in figure 4 also goes from at least two branches in case 10_1/2 to one in case 1_1/2. This results in a different Poincaré wave field in the majority of the domain.

5 Conclusions

We have performed a series of numerical experiments of a lock–release configuration exploring the effects that rotation and side walls have on the evolution of mode-2 ISWs. When the stratification has a single pycnocline form, naturally occurring mode-2 waves are quite likely to exhibit regions of overturning and hence our configuration is ideal for exploring the combined

effects of rotation and instability. Matching with the results of Maxworthy (1983), we observe that the leading ~~wave~~ wavefront becomes curved by rotation and that the dominant instability takes the form of two K-H ~~billows~~ billow trains at the crest of the wave, above and below the pycnocline center. By modifying the rotation rate we observe that as the rate of rotation increases, the instabilities become more energetic. This appears to be due to increased focusing of mass and the kinetic energy density along the focusing wall, especially in the early period of adjustment after the lock is released. Since these ~~type~~ types of shear instabilities are most commonly formed by large amplitude waves, this suggests that ~~channel trapped waves~~ Kelvin waves in a channel have a lower minimum amplitude threshold for instability generation and thus will have smaller amplitude waves compared to internal solitary waves in the open ocean.

These instabilities cause the leading wave to lose energy and thus higher rotation rates result in a faster decay in wave amplitude than cases with a lower rotation rate. The increased instability generation along the side wall also serves to create an asymmetry in the extent of mixing across the width of the tank. This effect could be observed in fjords or narrow lakes by making a careful comparison of mixing levels and wave amplitudes across the channel.

The high level of mass and kinetic energy along the focusing wall also resulted in the radiation of Poincaré waves, as previously described by Sánchez-Garrido and Vlasenko (2009). The Poincaré waves reflect off the opposing wall before returning to resonantly generate the secondary Kelvin wave along the focusing wall. When compared against an equivalent non-rotating case we found that this generation mechanism (through resonance) at higher rotation rates was completely different from the creation of secondary ISWs in a non-rotating reference frame. We referred to this wave as the secondary Kelvin wave. In addition to this, a Kelvin wave tail formed from the remains of the focused mass and energy along the wall. During propagation, we observed that the leading Kelvin wave appeared to lose energy to the both of these Kelvin waves, each of which became more energetic and thus faster. Eventually, these trailing Kelvin waves will overtake and surpass the leading wave, though we did not witness this phenomena. The results observed are fundamentally different than those seen without side walls. In the case without the side walls the leading wave energy is deposited into the trailing waves through dispersion eventually forming a wave packet. This packet has no span-wise variation. With side walls, the trailing waves are a fan of Poincaré waves that exhibit a complex interference pattern and hence have a span-wise structure. Furthermore, the energy of the leading wave is not continuously being lost to the primary trailing wave and hence this wave lives significantly longer, compared to the non-rotating case. ~~.~~

The results presented above suggest two clear avenues for future work. One avenue would focus on the rotation modified instability region. While in the above, clear evidence of transitional behaviour was presented, it is unclear to what extent a truly turbulent state was achieved. This is because trapping by the leading Kelvin wave is incomplete and turbulence may lose energy due to a spreading in space. Moreover, while the resolution of the numerical simulations was excellent for the full domain, a study that is focused on turbulent transition could optimize the domain and stratification parameters. For example, the domain could be shortened and the initial perturbation increased in size to increase the wave amplitude. While we have speculated that no-slip sidewalls would not fundamentally alter the shear instability, this remains to be confirmed by using a clustered, Chebyshev grid in the span-wise direction. A more likely mechanism to alter the shear instability is to raise the pycnocline such that the layers are of unequal depths to better approximate an oceanographic stratification.

A second possible avenue for future work would explore the effect of the span-wise extent. Figure 15 of Sánchez-Garrido and Vlasenko (2009) suggests that for wider domains, mode-1 Kelvin waves yield Poincaré wave trains whose focusing yields Mach stems on the far wall. We did not observe this phenomenon in our simulations, but it is possible that our span-wise extent was simply not large enough to achieve this. Of course, an experimental realization of our simulations would provide both a test of our results, and suggestions for future numerical studies that are most relevant to the experimentalist.

Competing interests. No competing interests are known.

Acknowledgements. Time dependent simulations were completed on the high-performance computer cluster Shared Hierarchical Academic Research Computing Network (SHARCNET, www.sharcnet.ca). DD and AC were supported by an Ontario Graduate Scholarships while MS was supported by an NSERC Discovery Grant RGPIN-311844-37157. Valuable comments by two anonymous reviewers are gratefully acknowledged.

References

Arthur, R. S. and Fringer, O. B.: Transport by breaking internal gravity waves on slopes, Journal of Fluid Mechanics, 789, 93–126, https://doi.org/10.1017/jfm.2015.723, 2016.

Benjamin, T. B.: Internal waves of permanent form in fluids of great depth, J. Fluid Mech., 29, 559, https://doi.org/10.1017/s002211206700103x, 1967.

Bourgault, D. and Kelley, D. E.: Wave-induced boundary mixing in a partially mixed estuary, Journal of Marine Research, 61, 553–576, https://doi.org/10.1357/002224003771815954, 2003.

Brandt, A. and Shipley, K. R.: Laboratory experiments on mass transport by large amplitude mode-2 internal solitary waves, Physics of Fluids, 26, 046 601, https://doi.org/10.1063/1.4869101, 2014.

Carr, M., Davies, P. A., and Hoebers, R. P.: Experiments on the structure and stability of mode-2 internal solitary-like waves propagating on an offset pycnocline, Physics of Fluids, 27, 046 602, https://doi.org/10.1063/1.4916881, 2015.

Coutino, A. and Stastna, M.: The fully nonlinear stratified geostrophic adjustment problem, Nonlinear Processes in Geophysics, 24, 61, https://doi.org/10.5194/npg-24-61-2017, 2017.

Cuypers, Y., Vinçon-Leite, B., Groleau, A., Tassin, B., and Humbert, J.-F.: Impact of internal waves on the spatial distribution of Planktothrix rubescens (cyanobacteria) in an alpine lake, The ISME Journal, 5, 580–589, https://doi.org/10.1038/ismej.2010.154, 2010.

Davis, R. E. and Acrivos, A.: Solitary internal waves in deep water, J. Fluid Mech., 29, 593, https://doi.org/10.1017/s0022112067001041, 1967.

Deepwell, D. and Stastna, M.: Mass transport by mode-2 internal solitary-like waves, Physics of Fluids, 28, 056 606, https://doi.org/10.1063/1.4948544, 2016.

Farmer, D., Li, Q., and Park, J.-H.: Internal wave observations in the South China Sea: The role of rotation and non-linearity, Atmosphere-Ocean, 47, 267–280, https://doi.org/10.3137/oc313.2009, 2009.

Fedorov, A. V. and Melville, W. K.: Propagation and breaking of nonlinear Kelvin waves, Journal of physical oceanography, 25, 2518–2531, https://doi.org/10.1175/1520-0485(1995)025<2518:pabonk>2.0.co;2, 1995.

Grimshaw, R.: Evolution equations for weakly nonlinear, long internal waves in a rotating fluid, Studies in Applied Mathematics, 73, 1–33, https://doi.org/10.1002/sapm19857311, 1985.

Grimshaw, R. H. J., Helfrich, K. R., and Johnson, E. R.: Experimental study of the effect of rotation on nonlinear internal waves, Physics of Fluids, 25, 056 602, https://doi.org/10.1063/1.4805092, 2013.

Hosegood, P. and van Haren, H.: Near-bed solibores over the continental slope in the Faeroe-Shetland Channel, Deep Sea Research Part II: Topical Studies in Oceanography, 51, 2943–2971, https://doi.org/10.1016/j.dsr2.2004.09.016, small and mesoscale processes and their impact on the large scale, 2004.

Katsis, C. and Akylas, T. R.: Solitary internal waves in a rotating channel: A numerical study, Physics of Fluids, 30, 297–301, https://doi.org/10.1063/1.866377, 1987.

Klymak, J. M. and Gregg, M. C.: Three-dimensional nature of flow near a sill, Journal of Geophysical Research: Oceans, 106, 22 295–22 311, https://doi.org/10.1029/2001jc000933, 2001.

Kundu, P. K., Cohen, I. M., and Dowling, D. R.: Fluid Mechanics, Academic Press, 5th edn., 2012.

Kuo, A. C. and Polvani, L. M.: Time-dependent fully nonlinear geostrophic adjustment, Journal of Physical Oceanography, 27, 1614–1634, https://doi.org/10.1175/1520-0485(1997)027<1614:tdfnga>2.0.co;2, 1997.

Lamb, K. G.: On boundary-layer separation and internal wave generation at the Knight Inlet sill, Proceedings of the Royal Society A: Mathematical, Physical and Engineering Sciences, 460, 2305–2337, https://doi.org/10.1098/rspa.2003.1276, 2004.

Maxworthy, T.: Experiments on solitary internal Kelvin waves, Journal of Fluid Mechanics, 129, 365–383, https://doi.org/10.1017/s0022112083000816, 1983.

Melville, W. K., Tomasson, G. G., and Renouard, D. P.: On the stability of Kelvin waves, Journal of Fluid Mechanics, 206, 1–23, https://doi.org/10.1017/s002211208900220x, 1989.

Mertz, G. and Gratton, Y.: Topographic Waves and Topographically Induced Motions in the St Lawrence Estuary, pp. 94–108, Springer-Verlag, https://doi.org/10.1007/978-1-4615-7534-4_5, 2013.

Moum, J. N., Farmer, D. M., Smyth, W. D., Armi, L., and Vagle, S.: Structure and Generation of Turbulence at Interfaces Strained by Internal Solitary Waves Propagating Shoreward over the Continental Shelf, Journal of Physical Oceanography, 33, 2093–2112, https://doi.org/10.1175/1520-0485(2003)033<2093:sagota>2.0.co;2, 2003.

Olsthoorn, J., Baglaenko, A., and Stastna, M.: Analysis of asymmetries in propagating mode-2 waves, Nonlinear Processes in Geophysics, 20, 59–69, https://doi.org/10.5194/npg-20-59-2013, 2013.

Renouard, D. P., D'Hières, G. C., and Zhang, X.: An experimental study of strongly nonlinear waves in a rotating system, Journal of Fluid Mechanics, 177, 381–394, https://doi.org/10.1017/s0022112087001009, 1987.

Salloum, M., Knio, O. M., and Brandt, A.: Numerical simulation of mass transport in internal solitary waves, Physics of Fluids, 24, 016 602, https://doi.org/10.1063/1.3676771, 2012.

Sánchez-Garrido, J. C. and Vlasenko, V.: Long-term evolution of strongly nonlinear internal solitary waves in a rotating channel, Nonlinear Processes in Geophysics, 16, 587–598, https://doi.org/10.5194/npg-16-587-2009, 2009.

Scotti, A. and Pineda, J.: Observation of very large and steep internal waves of elevation near the Massachusetts coast, Geophysical Research Letters, 31, L22 307, https://doi.org/10.1029/2004gl021052, 2004.

Shroyer, E. L., Moum, J. N., and Nash, J. D.: Mode 2 waves on the continental shelf: Ephemeral components of the nonlinear internal wavefield, Journal of Geophysical Research, 115, https://doi.org/10.1029/2009jc005605, c07001, 2010.

Stamp, A. P. and Jacka, M.: Deep-water internal solitary waves, Journal of Fluid Mechanics, 305, 347–371, https://doi.org/10.1017/s0022112095004654, 1995.

Subich, C. J., Lamb, K. G., and Stastna, M.: Simulation of the Navier-Stokes equations in three dimensions with a spectral collocation method, Int. J. Num. Meth. Fluids, 73, 103–129, https://doi.org/10.1002/fld.3788, 2013.

Terez, D. E. and Knio, O. M.: Numerical simulations of large-amplitude internal solitary waves, Journal of Fluid Mechanics, 362, 53–82, https://doi.org/10.1017/S0022112098008799, 1998.

Ulloa, H. N., de la Fuente, A., and Niño, Y.: An experimental study of the free evolution of rotating, nonlinear internal gravity waves in a two-layer stratified fluid, Journal of Fluid Mechanics, 742, 308–339, https://doi.org/10.1017/jfm.2014.10, 2014.

Ulloa, H. N., Winters, K. B., de la Fuente, A., and Niño, Y.: Degeneration of internal Kelvin waves in a continuous two-layer stratification, Journal of Fluid Mechanics, 777, 68–96, https://doi.org/10.1017/jfm.2015.311, 2015.

Vallis, G. K.: Atmospheric and oceanic fluid dynamics, Cambridge University Press, 1st edn., 2006.

Zhang, S., Alford, M. H., and Mickett, J. B.: Characteristics, generation and mass transport of nonlinear internal waves on the Washington continental shelf, Journal of Geophysical Research: Oceans, 120, 741–758, https://doi.org/10.1002/2014jc010393, 2015.